Additive manufacturing of pure copper: a review and comparison of physical, microstructural, and mechanical properties of samples manufactured with Laser-Powder Bed Fusion (L-PBF), Electron Beam Melting (EBM) and Metal Fused Deposition Modelling (MFDM) technologies

Thibaut de Terris, Thierry Baffie, Celine Ribiere

▶ **To cite this version:**

Thibaut de Terris, Thierry Baffie, Celine Ribiere. Additive manufacturing of pure copper: a review and comparison of physical, microstructural, and mechanical properties of samples manufactured with Laser-Powder Bed Fusion (L-PBF), Electron Beam Melting (EBM) and Metal Fused Deposition Modelling (MFDM) technologies. International Journal of Material Forming, 2023, 16 (4), pp.32. 10.1007/s12289-023-01755-2 . cea-04300147

HAL Id: cea-04300147

https://cea.hal.science/cea-04300147v1

Submitted on 22 Nov 2023

https://doi.org/10.1007/s12289-023-01755-2

Additive manufacturing of pure copper: a review and comparison of physical, microstructural, and mechanical properties of samples manufactured with Laser-Powder Bed Fusion (L-PBF), Electron Beam Melting (EBM) and Metal Fused Deposition Modelling (MFDM) technologies.

T. De Terris [a,1], T. Baffie [a], C. Ribière [a]

[a] Univ. Grenoble Alpes, CEA, LITEN, 17 avenue des Martyrs, 38000 Grenoble, France

ABSTRACT

Additive Manufacturing (AM) has become a relatively common material forming technology these days, just like conventional processes (such as casting or forging). It makes it possible to produce components with complex geometries, often unachievable with conventional manufacturing processes. In order to be able to choose the most suitable AM process (among all the existing ones) for a targeted application, this study aims to compare the physical and mechanical properties of pure copper parts manufactured with four different metallic AM processes: Laser-Powder Bed Fusion using infrared (1) or green (2) laser beams, Electron Beam Melting (3) and Metal Fused Deposition Modelling (4). It has been demonstrated that the parts fabricated with the processes involving a full melting of the material present better properties from all points of view (mechanical, electrical, and thermal properties). In addition, it has been shown that even if pure copper is a challenging material in AM due to its high reflectivity under infrared laser and high thermal conductivity, it is possible to manufacture quasi-dense parts (> 99%) with mechanical, electrical, and thermal properties comparable to those of pure copper produced by conventional processes.

---

[1] Corresponding author.
E-mail addresses : thibaut.de-terris@sfr.fr (T. De Terris, permanent address), thierry.baffie@cea.fr (T. Baffie), celine.ribiere@cea.fr (C. Ribière).

KEY WORDS

Additive Manufacturing, Pure copper, Microstructures, Tensile properties, Electrical conductivity, Thermal conductivity.

1. INTRODUCTION

Today, additive manufacturing (AM) makes it possible to produce metal parts with complex shapes, while optimizing their physical, mechanical, or thermal performances, and simplifying their manufacturing (e.g. reducing manufacturing and assembling steps, using only the necessary amount of materials, reducing lead time). However, certain metallic materials such as pure copper or noble metals (gold, silver) remain difficult to implement because of their intrinsic physical properties (good thermal conductivity, high optical reflectivity in the infrared). Therefore, there are currently few pure copper parts produced industrially by metallic 3D printing technologies, and still a limited number of studies on the subject, although the interest is growing from year to year. Recently, complex Cu parts targeting electrical, electromagnetic, or thermal applications have been developed, such as heat sinks [1,2], milli-channels heat exchangers [3], antenna [4], windings [5] or Radio Frequency Quadrupole [6].

The present study aims to first draw up a bibliographical review on the additive manufacturing of pure copper first, and then to compare four different AM technologies. The processes studied here are: (1) the Electron Beam Melting (EBM) process, (2, 3) the Laser-Powder Bed Fusion (L-PBF) process using a high-power infrared laser or using a green laser and (4) the Metal Fused Deposition Modeling (MFDM) process. Thereby, various pure copper samples were manufactured by four different subcontractors. The main goal was to realize an industrial blind-test in order to challenge what can be done at an industrial scale today and to validate the maturity level of the four processes and manufacturers. The comparison was based on the following characterizations:

- the chemical composition,

- the surface roughness,
- the density,
- the microstructure,
- the mechanical behavior (tensile properties, micro hardness),
- the electrical conductivity,
- the thermal conductivity.

2. PROCESSES STUDIED

The ISO/ASTM 52900:2015 standard defines additive manufacturing (AM) as the “process of joining materials to make parts from 3D model data, usually layer upon layer” [7]. Nowadays, different metal AM technologies are available and are classified into two main categories called "direct" or "indirect" processes.

The 3D parts manufactured using so-called "direct" technologies are based on the complete melting of the raw material during the process (change from the solid state to the liquid state of the metal). They do not necessary require any post-treatment to obtain the final parts.

Conversely, the parts produced with so-called "indirect" technologies are initially based on the printing of a mixture between the raw metallic material (in powder form) and a polymer carrier (or binder) which is used to consolidate the filler material. The parts thus obtained - qualified as "green parts" - must be subjected to a heat treatment cycle called "debinding-sintering" in a second step, which aims to remove the carrying/binding polymer and densify the metallic powder to obtain the final parts. The major difference of these technologies compared to the direct ones is that there is no full melting of the metal.

Note that an exception is made for the Cold-Spray Additive Manufacturing (CSAM) process and the Selective Laser Sintering (SLS) process which are considered as "direct" processes although the powder is not melted (or partially). Indeed, the material formed does not require any particular post-treatment (debinding, sintering) comparable to those involved in the "indirect" processes.

This section aims to describe each metal AM technologies involved in this study and given in Figure 1.

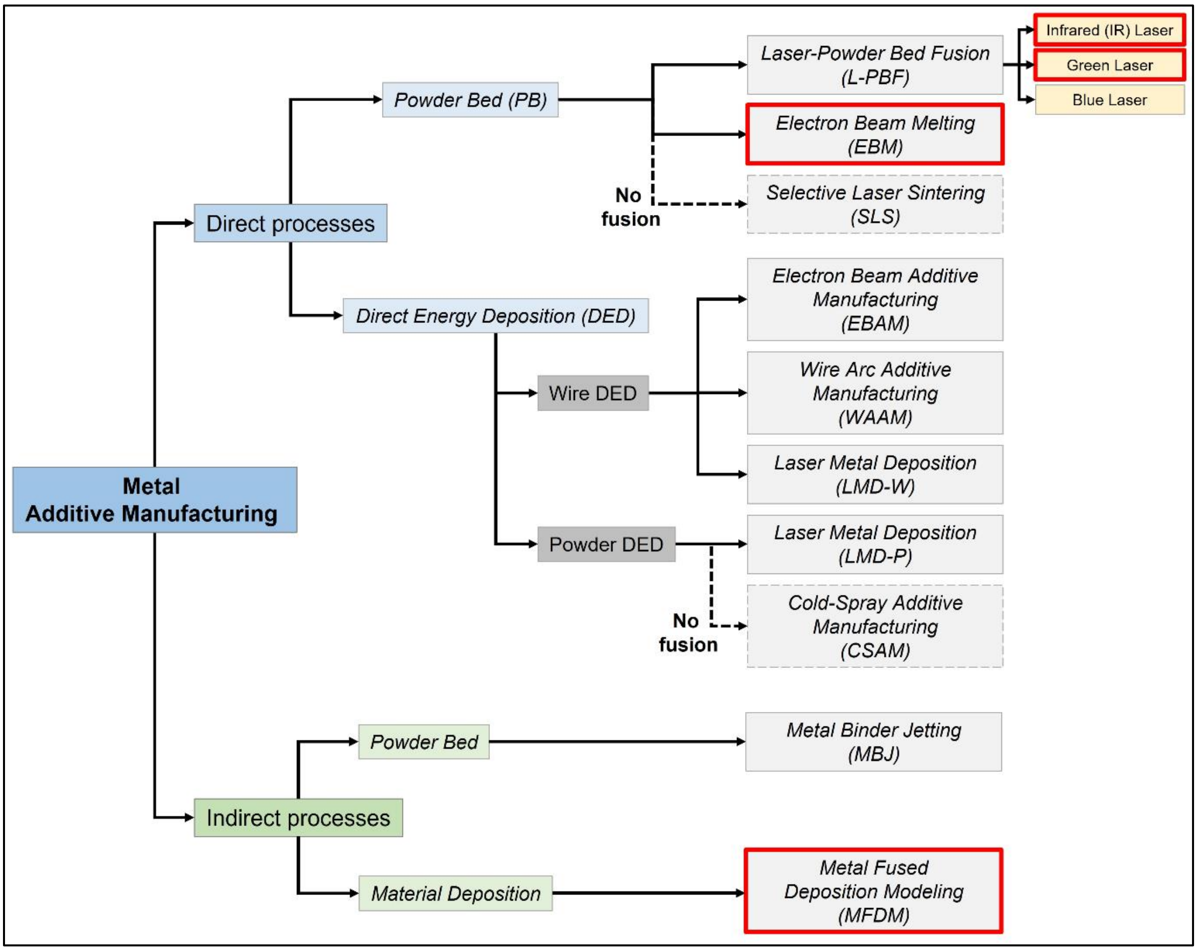

Figure 1 – The main current commercial metal additive manufacturing processes able to produce copper parts. The processes framed in red indicate those studied in this article.

2.1. Laser-Powder Bed Fusion (L-PBF) process

The Laser-Powder Bed Fusion (L-PBF) process consists in superimposing layers of a metallic powder (particles size typically between 10 and 45 µm) selectively melted by a laser successively, one after the other, as described in Figure 2. The process is broken down into different stages as indicated below, after having properly prepared a CAD file and generated the associated STL file.

1. A thin layer (typically 30 µm) of metallic powder is spread on a build plate using a scraper or a roller.
2. A laser beam, driven by two mirrors, selectively melts this powder layer, generating a 2D section of the part after solidification.
3. The build plate is lowered, and a new powder layer is spread over the previous one and then melted.
4. The laser selectively melts the new spread powder layer, generating the next 2D section of the part after solidification. Each melting step is carried out so that the previous layer is remelted to ensure good metallurgical cohesion between the layers.
5. Steps 3 and 4 are repeated in this way until the end of the process. Then the build plate is raised, the un-melted powder is removed, and the parts are cut from the build plate. Optionally, parts may undergo finishing post treatments (heat treatments, sandblasting, machining, etc.).

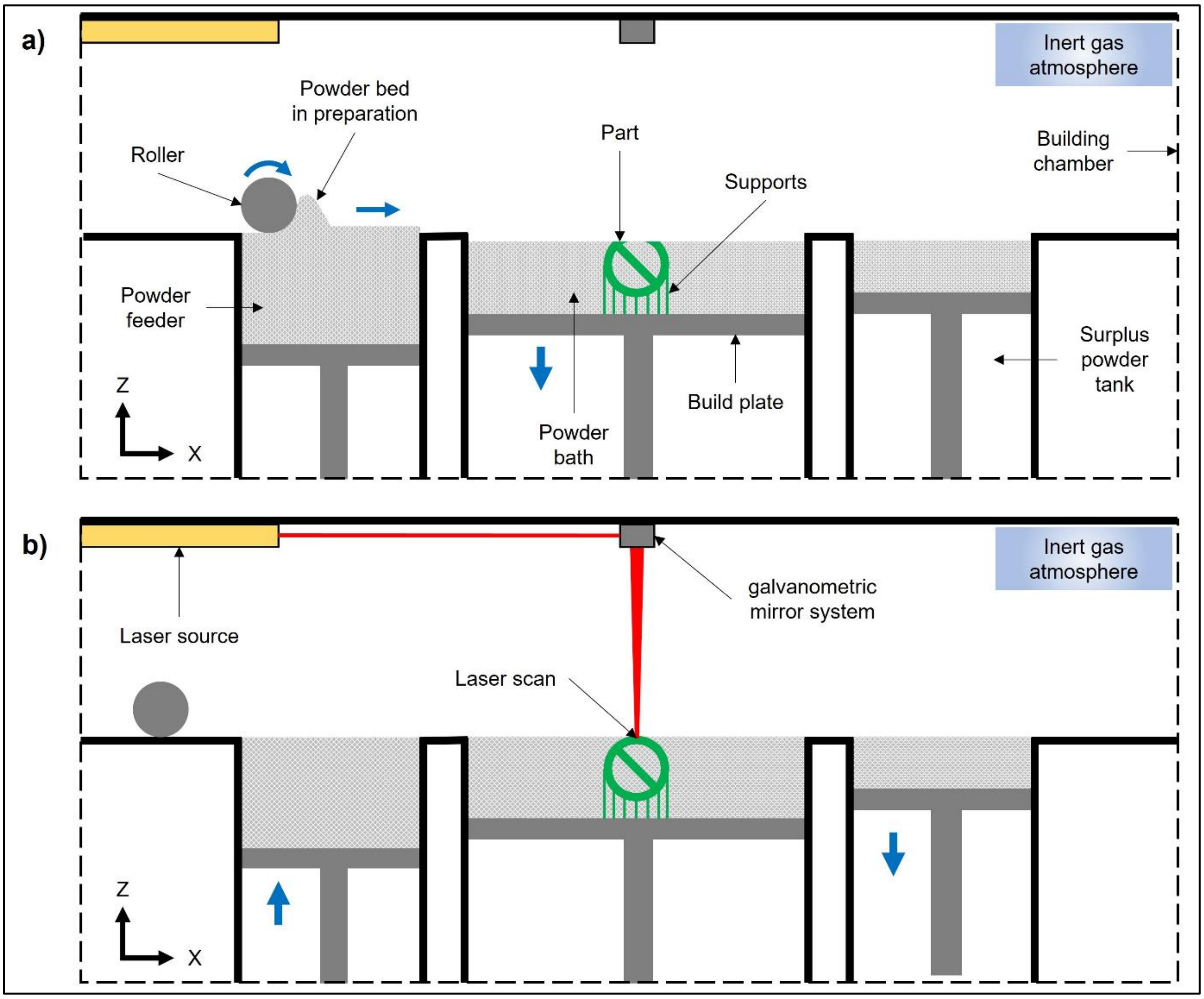

Figure 2 – Laser-Powder Bed Fusion (L-PBF) process principle: (a) powder layering, (b) laser melting.

The L-PBF process is carried out under a gas protection (mainly argon or nitrogen). The role of this gas flow is multiple. First, it is used to protect the parts from oxidation due to an imperfectly controlled chamber atmosphere and from the liquid or powder ejecta inherent in the process (to make them fall out of the powder bed). Moreover, it allows to shear the vapor plume (to avoid as much as possible its interaction with the laser), and to protect the laser optics (to limit the deposition and condensation of vapors on the windows).

Most L-PBF machines use Yb: YAG or Nd: YAG fiber infrared lasers with a wavelength λ_{IR} of 1080 nm. Two types of laser beams spatial distributions can be easily offered: a Gaussian distribution with small spot diameter (80 µm) using a single-mode laser source or 'Top Hat' distribution with large spot diameter (500-700 µm) using a multimode laser source. But some machines are now equipped with a so-called "green" laser with a wavelength λ_G of 515 nm. At this lower wavelength, the absorption of the laser radiation by the solid-state material is increased, as shown by Sinico et al. [8] for example, which improves the material melting. This type of laser is specially used for reflective materials, such as copper and its alloys or precious metals (gold, silver). Figure 3 shows the spectral absorptance of various metals.

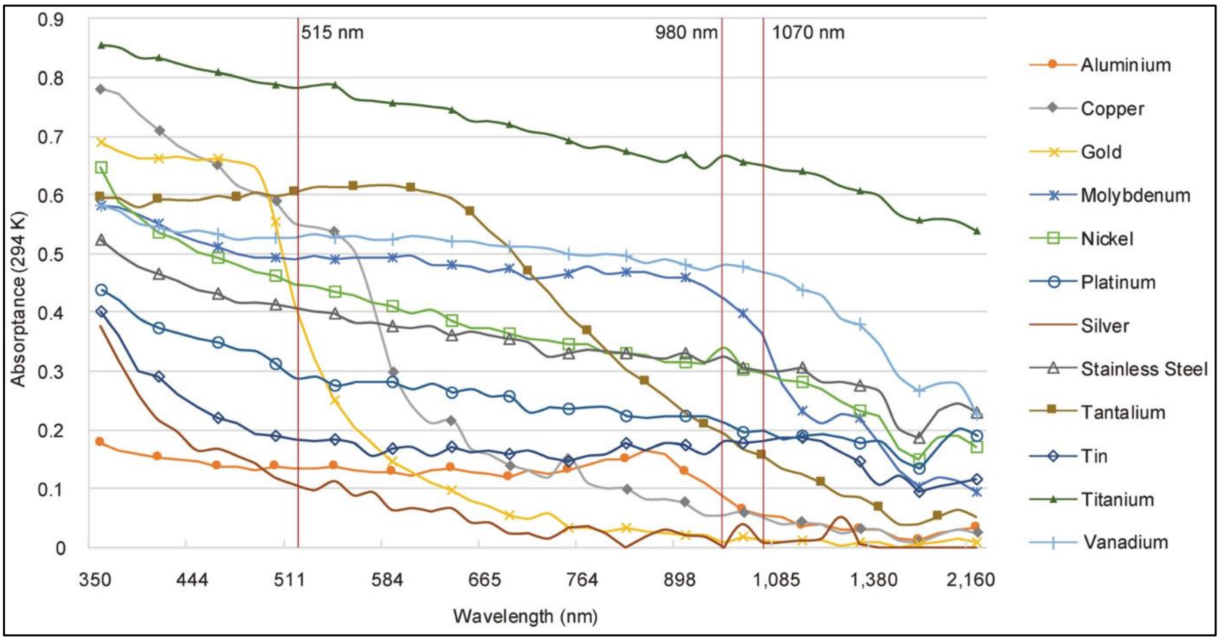

Figure 3 – Absorptance for various high-purity metals according to the wavelength. Figure from Himani Siva Prasad* et al. *[9] reproduced under the terms of the Creative Commons CC BY license. No modifications were made.

In our present study, samples manufactured with a high-power (i.e. ≥ 500 W) “infrared” laser HPIR ($\lambda_{IR} \approx 1064$ nm) and a “green” laser ($\lambda_G \approx 515$ nm) are compared to characterize the influence of the type of laser on the quality of the resulting parts, and particularly in terms of density, microstructures, mechanical, electrical and thermal properties.

2.2. Electron Beam Melting (EBM) process

The Electron Beam Melting (EBM) process is comparable to the L-PBF process (Figure 4). It is based on the superposition of layers of a metallic powder, selectively melted one after the other, as described previously, but the fusion is ensured by a high-power electron beam (typically 1 to 3 kW) instead of a laser.

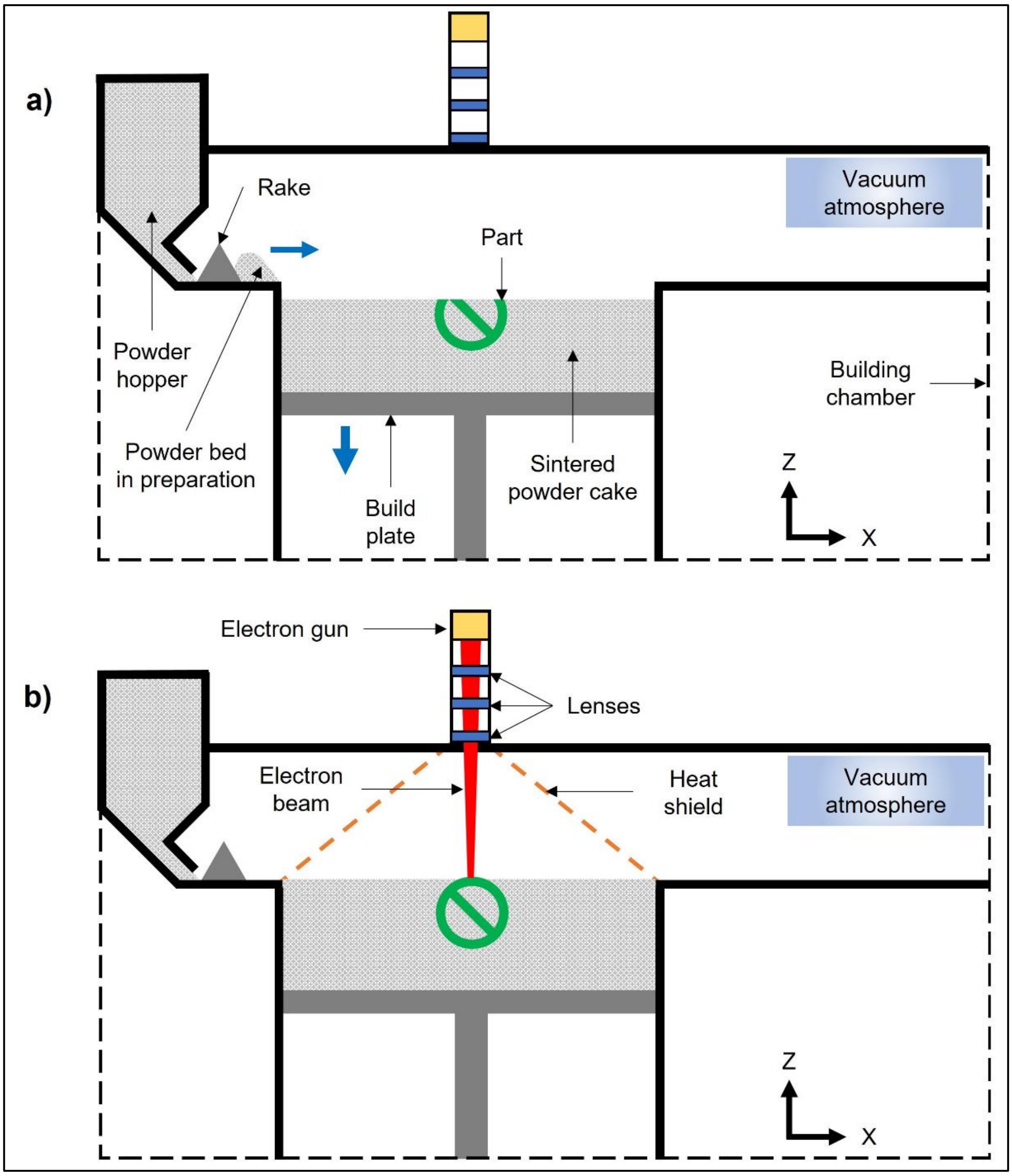

Figure 4 – General principle of the Electron Beam Melting (EBM) process: (a) powder layering, (b) electron beam melting.

The use of an electron beam implies that this process is carried out under vacuum (10^{-3} mbar), unlike the L-PBF process which operates under a protective atmosphere. It should be noted that the particle size of the metallic powder used in this process is higher (40 – 100 µm) than for the L-PBF process. This makes it possible to work with higher layer thicknesses (50 – 150 µm) and to gain in productivity. However, these two factors will contribute to the surface roughness increase compared to the parts produced by L-PBF. In addition, at each layer, the powder bed is first preheated and sintered up to 1100 °C using a defocused before being selectively melted. This eliminates the use of supports to hold the parts on the build plate and prevents the collapse of the down-skin surfaces. Moreover, this sintering step makes it possible to maintain the powder bath and the parts at a high temperature, which will contribute to limit the thermomechanical residual stresses in the parts.

2.3. Metal Fused Deposition Modelling (MFDM) process

The Metal Fused Deposition Modeling (MFDM) process is derived from the Fused Deposition Modeling process, which originally operates with polymers materials. As described in Figure 5, this process consists in the extrusion of a filament on a build plate to form a bead of material. The filament used is a mixture of a metallic powder (pure copper in our case) and a polymer carrier, which forms the feedstock in a wire form. The juxtaposition and the superposition of the raw strands makes it possible to manufacture a part. These parts cannot be used as such, and the process is followed by a thermal cycle to complete the manufacturing. Indeed, the “green parts” need to be heat treated with a curing cycle (evacuation of the organic compounds) followed by a sintering step to densify the material and get the parts with their final properties. The sintering step leads to a size reduction (shrinkage) of the parts. Considering copper extrusion, Singh et al. [10] revealed an approximately isotropic shrinkage around 13 %, whereas Ren et al. [11] measured a shrinkage of ~ 21% along the 3 directions. The CAD model must therefore take this aspect into account to obtain parts with the right dimensions at the end of the process.

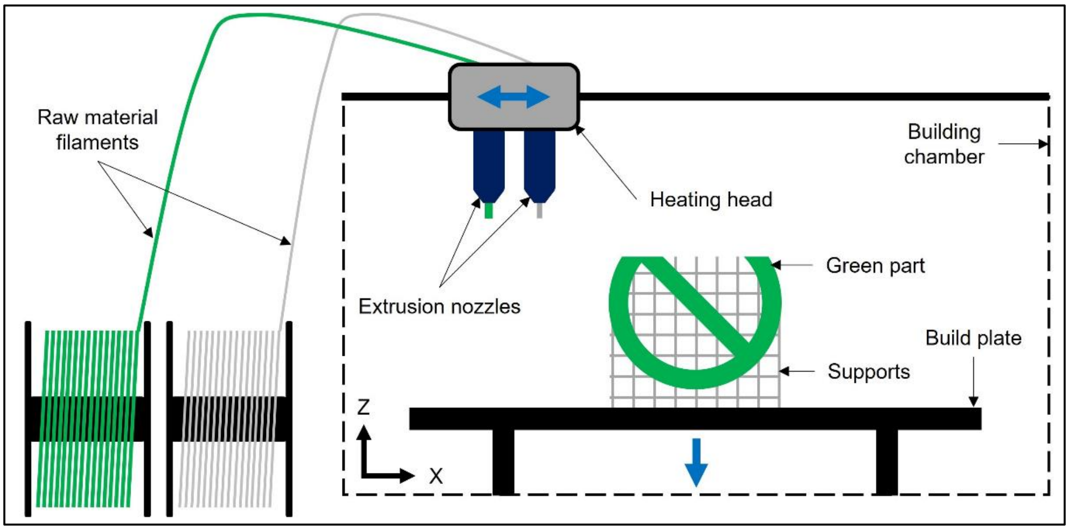

Figure 5 – Metal Fused Deposition Modeling (MFDM) process principle.

3. BIBLIOGRAPHICAL REVIEW

3.1. Wrought copper grades and associated electrical, thermal, and mechanical properties

The applications of pure copper take generally advantage of its high electrical conductivity or its high thermal conductivity. There are different grades depending on their purity. For Electrolytic Touch-Pitch (ETP) wrought Cu (Copper content higher than 99.9 wt.% and Oxygen content between 200 and 400 ppm), the electrical conductivity is equal or higher than 58 MS/m or 100% IACS, i.e. International Annealed Copper Standard, at 20°C [12]. Oxygen Free (OF) wrought Cu (Cu > 99.95 wt.% without oxygen) presents the same values. For Oxygen Free Electronic (OFE) wrought Cu (Cu > 99.99 wt.% without oxygen), the electrical conductivity is equal or higher than 58.6 MS/m or 101% IACS at 20°C. These two last grades are well suited for scientific applications working under ultra-high vacuum. The minimum guaranteed values of thermal conductivity at 20°C for Cu-ETP (or Cu-OF) and Cu-OFE are, respectively, 388 W/m.K and 391 W/m.K [12]. It is well known that few tens of ppm of impurities such as Phosphorus or Iron or a few hundred ppm of Chromium, Tin or Nickel in solid solutions will highly decrease both conductivities.

The mechanical properties of wrought pure copper do not depend on the grade; in an annealed state, Ø25 mm rods give the following same typical values: hardness of 40 HRF (~ 55 HV_{10}), yield strength of 69 MPa, ultimate tensile strength of 220 MPa, elongation at break of 55 % [12].

3.2. Additive manufacturing of copper parts

Several reviews relative to AM of pure Copper have been already published during the five past years. Especially, [13] give an exhaustive table allowing to compare the mechanical and physical properties of Cu parts obtained by L-PBF, EBM and MBJ processes. The same year, [14] have published an overview of research advances on copper manufacturability via powder-based AM processes. Pure Copper parts have been shaped by several AM processes, either direct processes, like Laser Powder Bed Fusion (L-PBF) using infrared lasers [15] or green lasers [16], Electron Beam Melting (EBM) [17], Laser Direct Energy Deposition (LDED, or Laser Metal Deposition using Powder LMD-P) [18], Cold Spray Additive Manufacturing (CSAM) [19], Wire Arc Additive Manufacturing (WAAM) [20] or indirect processes, such as Metal Binder Jetting (MBJ) combined with Hot Isostatic Pressing (HIP) [21] or Metal Fused Deposition Modelling (MFDM) [22]. The following bibliographical review presents an overview of the additive manufacturing of copper parts according to their targeted size: large parts (> 0.5 m^3), intermediate parts (0.01 to 0.5 m^3) and small parts (< 0.01 m^3).

3.2.1. Additive manufacturing of large size copper parts

LMD-P, WAAM and CSAM processes are targeting large parts, from 0.5 m^3 to tens of m^3. Their building speed ranges from 100 to 1000 cm^3/h, the dimensional accuracy of built parts is rather low (± 0.2 mm) and the achievable complexity of parts is quite limited. Up to now, scarce data are available regarding pure Cu parts produced by these processes. For a CSAM part in as-built state, Huang et al. [19] reported a density of 99.2% and measured an electrical conductivity of 42 MS/m (73% IACS) at room temperature. The main problem they reported seems to be the extremely low elongation at rupture (0.8% ± 0.2) of their part. This information is confirmed by [23] with a result of elongation at rupture of 0.1%. Concerning the LMD-P process [18], the elongation of pure Cu (with a measured density of 99.9%) at room temperature is much higher (19-21%). However, neither electrical nor thermal conductivity have been measured in this study. Using the WAAM process, Williams et al. [24] measured an electrical conductivity of 102% IACS in a wall manufactured using an electrical wire, and at a 45 mm height from the substrate, although they indicate the presence of porosity (rate not specified).

3.2.2. Additive manufacturing of intermediate size copper parts

EBM and L-PBF processes are generally targeting parts up to 0.5 m^3. EBM allows to produce parts with rather small building rate (25 to 100 cm^3/h) and similar dimensional precision to LMD-P or CSAM (± 0.2 mm). Copper inductors produced by EBM are offered commercially since 2017 [25,26]. Thanks to the high energy absorptivity of the electron beam and the pre-heating step, copper is easily shaped by EBM and parts densities of 99.95 % can be reached [27]. Depending on the process conditions, electrical conductivity of as-build Cu parts is higher than 56.8 MS/m (98% IACS) [17] and can reach 59.2 MS/m (102% IACS) [27], which corresponds to the values of Cu-OFE. At room temperature, thermal conductivity reaches values over 400 W/m.K [17]. With EBM, mechanical properties are close to the ones of an annealed wrought copper, with, whatever the building orientation, hardness values over 50 $HV_{0.5}$, Yield Strength over 60 MPa, Ultimate Tensile Strength over 180 MPa and elongation at rupture over 47 % [17,27].

Several variants of the L-PBF process have been developed recently; the reference process, which is mainly used in industry, uses infrared (IR) lasers (wavelengths of 1064 to 1080 nm) and laser powers up to 500 W [28]. New processes employ either high-power IR lasers, i.e. power equal or higher than 500 W [29,30], femtosecond IR lasers [31], green lasers (wavelength of 515 or 532 nm) [32,33], or blue lasers (wavelength of 450 nm) [34,35].

Using a IR laser at 500 W and highly pure Cu powder (99.99 % purity, with Sn content below 100 ppm, Fe below 10 ppm, Ni and Cr below 10 ppm and O below 115 ppm), Jadhav et al. [28] reached a 99.8% density and an electrical conductivity of 94% IACS. Surprisingly, relative densities (ρ) obtained in other studies using high-power IR lasers (≥ 500 W) were lower ; ρ > 98 % [30], ρ = 98.7 % [29] or ρ = 96.6 % [36]. These studies involving the use of high powers (up to 1000 W) and high Volumetric Energy Densities (VED, J/mm^3) to stabilize the melt pools, such melting conditions induced a keyhole-mode fusion of the copper and associated keyhole defects (entrapped gas, as shown by [29,36], as explained by [28]. Copper parts produced by L-PBF using high power IR lasers are offered commercially since recently [37,38]. According to the datasheets, minimal density of 8.9 g/cm^3 (i.e. 99.3 %), electrical conductivity of 57-58 MS/m (98.3-100 % IACS) and thermal conductivity of 400 W/(m.K) can be expected from the delivered parts.

Using a low-power IR laser makes it generally difficult to produce dense pure Cu parts, as shown by various authors. [39] reached densities from 93,3 % (using a pure copper powder) to 98.3 % (using a copper with 0.43 wt.% impurities). Playing on the scan speed and the hatching distance, [1] manufactured parts with densities ranging from 70 % to 95 %. Using a fine PSD powder (5-25 µm) and investigating the laser power, scan speed and hatching distance parameters, Qu et al. [40] reached densities up to 99.5 %. This density issue is due to the low absorptivity of the powder bed and the high thermal conductivity of copper, which results in high cooling rates and in deleterious consequences on the stability of the melt pool. Defects, such as lack of fusion pores, associated with these phenomena, impacts negatively the electrical, thermal, and mechanical properties. One way to increase the powder absorptivity is to engineer the surface of the particles; this has been studied by different routes: by a controlled surface oxidation [15,41] ; or by the grafting of carbon nanoparticles [42] or graphene microflakes [43], or by chemical deposition of nickel [44]. Even with laser powers of 500 W [15] and 725 W [42] respectively, none of the two first approaches used by Jadhav et al. succeeded in reaching electrical conductivity of 58 MS/m. No electrical results have been published by

[43]. With 0.4 wt.% Ni, Zheng et al. reached only 30.9 MS/m (53.3% IACS), which can be explained by the solubility of Ni in Cu and probably the low purity of the initial Cu powder (99.7%) [44].

Another route used to increase the laser absorptivity by the powder consists in alloying copper with small amounts of additional elements before powder atomization; Jadhav et al. have evaluated the effect of 0.28 wt.% Tin addition [45]. Despite a 99.6% relative density, the electrical conductivity was only 80% IACS, which is explained by the decreasing effect of Sn on the Cu conductivity. The effect of Chromium addition was also studied by three different process routes; a Cu-0.89wt.%Cr powder was heat treated under nitrogen to form a Cr nitride, which lead to a relative density of 99.1% and an electrical conductivity of 81% IACS [46]. The powder of the same alloy was also grafted with Carbon nanoparticles and heat treated at 750°C, thus forming a Cr carbide; this process leads to 99.1% relative density and 93% IACS electrical conductivity [47]. Finally, a Cu-0.3wt.%Cr powder, with a relative high oxygen content (0.14 wt.%) was grafted with 0.05 wt.% of carbon nanoparticles; L-PBF parts were only 98.7% dense and their electrical conductivity was 87% IACS [48]. It is worth noting that, whatever the route used for surface modification, a minimum laser power of 500 W was necessary to reach the highest relative density.

Most of the IR lasers employed for L-PBF are continuous wave (CW) and pulsed laser systems with ns pulse duration. Kaden et al. [31] have tested ultrashort pulse lasers (UPS) using 500 fs laser pulses at MHz repetition rates. However, the copper parts produced up to now are highly porous.

Bulk copper is highly reflective to wavelengths in infrared and near infrared regions (3-5 %), while its absorptivity becomes 30-35 % at green (515-532 nm) and 45-50 % at blue (450 nm) wavelengths [49]. Using a blue diode laser on an experimental bench, Hori et al. [34] fabricated Cu parts with a 99.1% relative density. Takenaka et al. [35] further improved the bench but, for the moment, relative densities of Cu parts remain below 99% and no electrical properties have been published.

Publications relative to the use of green lasers in L-PBF for pure copper are currently rare, but this type of laser has been initially developed for Cu welding [50]. Using a pulsed active fiber laser from IPG Photonics (532 nm) at an average power of 50 W, Demir et al. [51] produced L-PBF Cu parts with 99.6% relative density, but no measurement of their electrical properties has been reported. Copper parts produced by L-PBF using a CW fiber green laser (515 nm) are offered commercially since recently [16,52]. Nordet et al. [33] evaluated the interest of the high power (1 kW) CW green laser (TruDisk 1020) used by Trumpf in their L-PBF machine through absorptance measurements up to 800 W for different Cu states (powder bed for single and multiple tracks, liquid and keyhole). According to the datasheet of Trumpf and measurements performed independently by Gruber et al. [32], a mean relative density of 99.8% and an electrical conductivity of 58 MS/m (100% IACS) can be expected from the delivered parts. The announced tensile properties are close to the ones of an annealed wrought copper, with, whatever the building orientation, Yield Strength over 125 MPa, Ultimate Tensile Strength over 180 MPa and elongation at rupture over 47 % [32].

3.2.3. Additive manufacturing of small size copper parts

MBJ and MFDM processes are targeting small complex components with size below Ø150 mm. Commercially announced building speeds are in the 100-1000 cm^3/h range and dimensional precision is comparable to the one of Metal Injection Moulding (MIM) process (± 0.05 to 0.1 mm). Copper parts produced by MBJ have been recently released on the market [53,54]; however, their as-sintered relative density, which is 96-97% of the theoretical density of Copper, leads to an electrical conductivity 52 MS/m (90% IACS). This value corresponds to the highest value measured by Yegyan Kumar et al. [21] on samples obtained by the combination of a bimodal particle size distribution (73 wt.% of a powder having a D50 of 30 µm and 27 wt.% of a powder with D50 of 5 µm) and a HIP cycle at 1075°C and 206MPa. Despite these very favorable conditions for densification, the relative density remains lower than 97.5%.

MFDM processes include several variants which can be categorized according to the shape of the filler material (filament, pellet, slurry, paste, suspension); these processes are targeting small parts (size below Ø150 mm); their building speed ranges from 1 to a few cm^3/h; the dimensional precision of built parts is very low (± 0.4 to 1 mm) and the complexity of parts is quite limited. Copper parts produced by MFDM processes using either filaments (Atomic Diffusion Additive Manufacturing, ADAM) [55] or rods (Bound Metal Deposition, BMD) [56] are offered commercially since recently. The announced relative density and electrical conductivity are, respectively, 98% and 49 to 49.4 Ms/m (84-85% IACS). Publications relative to the use of MFDM (or associated processes based on material extrusion) for pure copper are still few and performances relatively lower than the ones announced commercially; relative densities range from ~89 %[22] to 94.5% [57], with intermediates values around 90 % [58,59]. The maximal electrical conductivity is given by [57]: 86.1 % IACS (49.4 MS/m).

4. SAMPLES DESCRIPTION AND ASSOCIATED CHARACTERIZATIONS

For each of the four additive manufacturing processes studied, subcontractors manufactured different samples to assess the capacities of each process. The Table 1 shows the samples requested from subcontractors and the associated characterizations while Figure 6 illustrates an example of a build plate with a series of parts manufactured by L-PBF and by MFDM.

Properties to characterize		Samples	Dimensions (mm)	Quantities
Surface roughness		Cubes	10×10×10	4
Density				
Micro-hardness				
Microstructures				
Chemical composition				
Electrical conductivity		Vertical cylinders (i.e. the axis is parallel to the building direction BD)	Ø18 × 22	3
Thermal conductivity			Ø11 × 11	3
Mechanical tensile properties	Vertical orientation	Vertical cylinders (i.e. the axis is parallel to the building direction BD)	Ø10 × 50	6

at room temperature and 250 °C	45° orientation	Parallelepiped inclined at 45 ° (with respect to the building direction BD)	13*13*60	5

Table 1 – Details of the properties characterized in this study, and the associated samples required in each additive manufacturing processes.

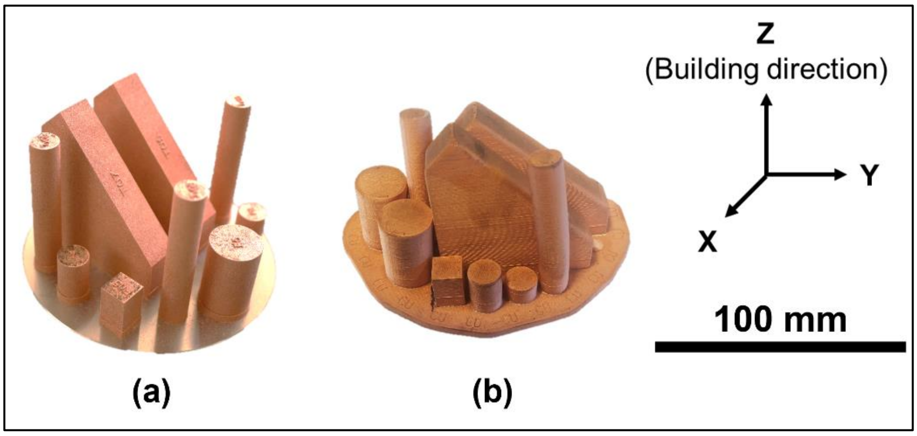

Figure 6 – Example of the samples manufactured with the Laser-Powder Bed Fusion (L-PBF) process equipped with a green laser (a) and the Metal Fused Deposition Modeling (MFDM) process (b). Tensile specimens inclined at 45 ° have "solid" supports to prevent them from collapsing during manufacturing.

It should be noted that our request to the manufacturers was to deliver parts as manufactured without unnecessary post-treatment. All manufacturing being subcontracted, no information on the filler material (powders, filament) nor data concerning the implementation of the processes (manufacturing parameters, post-treatments, or finishing steps) have been communicated by the manufacturers.

5. CHARACTERIZATION AND ANALYSIS METHODS

5.1. Chemical composition analyzes

The Inductively Coupled Plasma (ICP) and Instrumental Gas Analysis (IGA) methods were used by an industrial subcontractor to analyze the chemical composition of the samples. The contents of the following elements were measured: C, O, S, P, Fe, Sn Si and Ti. Results correspond to the average of two or three measurements.

5.2. Surface roughness measurements

Surface roughness measurements were performed with an Alicona InfiniteFocus, an optical 3D measurement system, at x10 magnification (pixel size: 0.88 µm; image size: 1.43*1.08 mm). Each dedicated sample was characterized on three different sides, as shown in Figure 7 below. Two different measurements were performed according to [60] on each side to qualify the Ra, Rz, Rp and Rv values of the surfaces. The Ra value corresponds to the arithmetical mean of the absolute values of the profile deviations from the mean line of the roughness profile, the Rz value corresponds to the average peak-to-valley height of the roughness profile and the Rp and Rv correspond, respectively, to the maximum peak height of the roughness profile and to the maximum valley depth of the roughness profile. For each manufacturing process, the results presented in this study are the average of the values obtained on the vertical (XZ and YZ sides) or horizontal (XY side) faces of the 4 samples analyzed (i.e. 16 vertical measurements and 8 horizontal measurements).

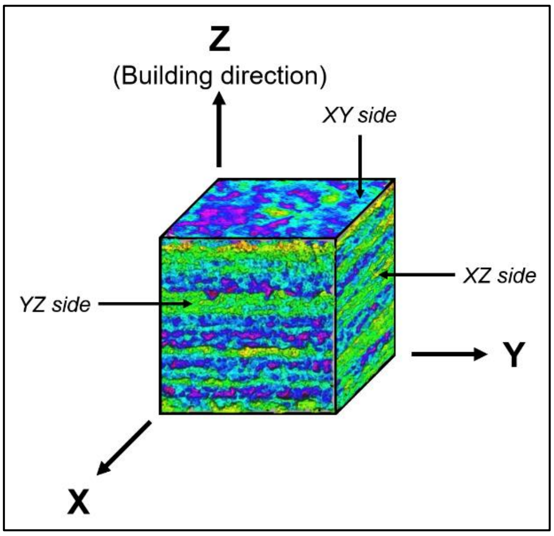

Figure 7 – Schematic representation of a cube dedicated to surface roughness analyzes.

5.3. Density measurements

5.3.1. The Archimedes' method

Relative density measurements were performed by the Archimedes' method on a Mettler AE200 balance equipped with a density measurement kit using anhydrous ethanol, following the method described by many authors, such as De Terris et al. [61] who show that this is a relevant method to characterize the density of parts made by additive manufacturing. In our case, the samples were analyzed *as-manufactured*, i.e. the surfaces remained raw (unpolished). The exact fluid density was regularly measured with the same principle, using a calibrated quartz sample of precisely known density as a reference (its density being precisely known). Before each measurement in ethanol, samples were systematically immersed in the fluid and placed in a dynamic vacuum chamber for 20 minutes. This makes it possible to eliminate all air bubbles which could be trapped in the anfractuosities of the rough surfaces, and also to impregnate with ethanol all the open porosities (i.e. opening outwards as shown in Figure 8). Here, the relative density of the samples was calculated considering that the theoretical pure copper density at 20 °C is 8.94 g/cm^3 [12].

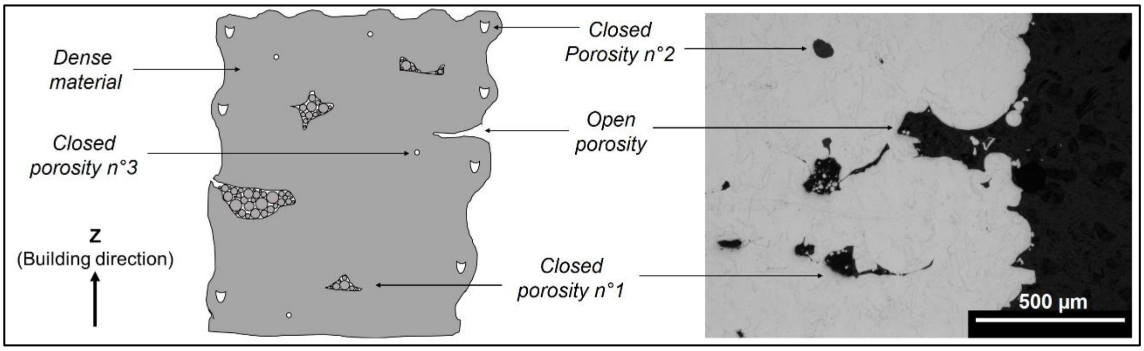

Figure 8 – Schematic and micrographic sections showing the different types of porosities present in additive manufactured parts. The so-called "closed" porosities do not open out to the outside while the so-called "open" porosities open outwards. The porosities with coarse geometries and containing unmelted powder are called "lack of fusion" (porosity n°1), while quasi-spherical (porosity n°2) or spherical (porosity n°3) porosities are related to the presence of gas entrapped in the material.

This method makes it possible, in the case of samples having open porosities, to also quantify the amount of "open" porosities (called "open porosity" rate thereafter in this study), using a third measurement step (which consists of weighing the sample in air after the immersed measurement and a short surface wiping). Results are the mean of 5 independent measurements for each sample.

5.3.2. Micrographic cross-sections

Another way to characterize the relative density of additive manufactured sample is the image-analysis of micrographic cross-sections. For each process, two samples were cut along an XZ plane, and the reaming two samples were cut along an XY plane (Figure 9-a).

Each sample section was hot-mounted within a phenolic resin, and then polished to reach a "mirror" polished surface. The samples were polished with SiC papers down to grit 4000 ; then, diamonds suspensions were used down to 1µm grain size. A suspension of colloidal silica (OPS) was then used for the finishing step. With an optical microscope (InfiniteFocus from Alicona) at magnification x10 (pixel size = 0.88 µm), a mosaic was obtained for each sample section (Figure 9-b). This image was converted to a shade of gray and then binarized; the pores turned black and the metal white. The last step was to color in red the larger black area, which actually corresponds to the resin (Figure 9-c,d).

Then, by an automatic processing step on ImageJ software, it was possible to measure the number of black pixels *NB* (corresponding to pores) and white pixels *NW* (corresponding to metal). The ratio [*NW* / (*NB* + *NW*)]*100 gives the relative density of each micrographic cross-section in %. By applying this analysis to each section (2 per sample), it was possible to obtain an average relative density value over 8 different analyzes per process.

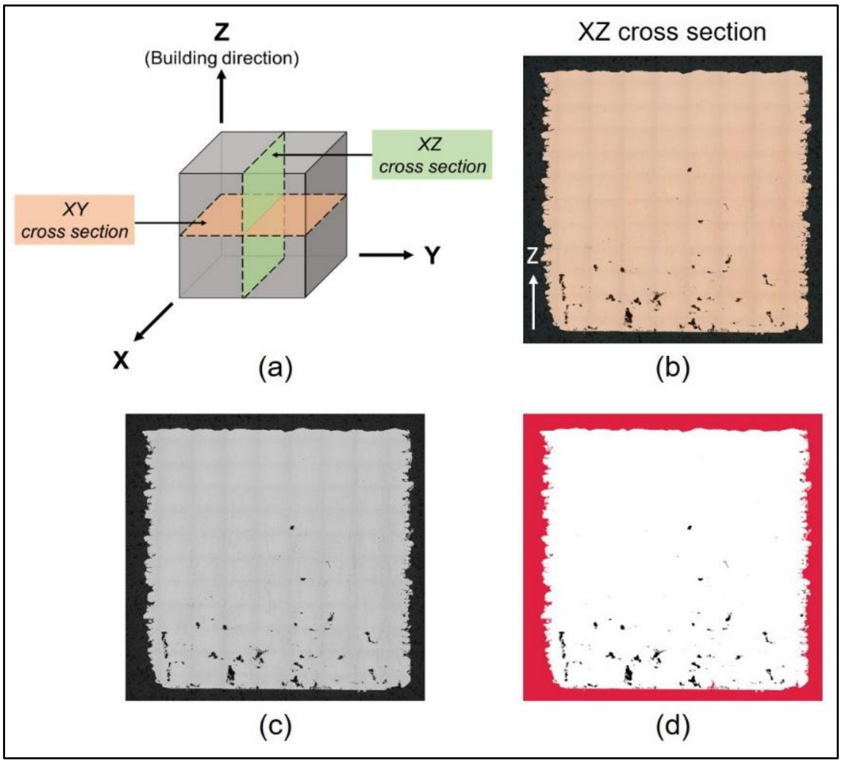

Figure 9 – Illustration of the two cross sections studied for each process (a) and image-analysis steps: (b) XZ micrographic mosaic cross section, (c) conversion to a shade of gray image and (d) binarization and counting of white and black pixels. In this example, the relative density is 99 %.

5.3.3. Helium pycnometry

The real density (ρ) of each sample was measured by the helium pycnometry method (described by [61]) on an AccuPyc II 1340 device from Micromeritics equipped with a 1.34 cm^3 cylindrical measurement cell. These measurements were carried out on the cylindrical samples used to calculate the thermal conductivity (cf. Table 1), as these density measurements results were used in the thermal conductivity equation (cf. equation (1)). The ratio between the measurement cell volume (1.34 cm^3) and the samples volume (estimated to 1.04 cm^3) allows to maximize the reliability of the results. The results obtained for each sample are an average of 150 measurements at room temperature (20 °C).

5.4. Microstructure analyzes

In this study, the microstructures were revealed using two different methods. The first one, simple and fast, consists in the use of a chemical reagent in order to have a first overview of the morphologies and sizes of grains with observations in optical microscopy. The second one, more difficult to implement, consists in carrying out Electron Backscatter Diffraction (EBSD) analyzes with a scanning electron microscope (SEM).

5.4.1. Chemical reagent

The chemical reagent used to reveal the microstructures was adapted from relevant standard dedicated to the micro-etching of metals and alloys [62] (etchant n° 30). It is a fresh mixture composed of 50 mL of distilled water, 50 mL of an ammonium hydroxide solution and 20 mL of a hydrogen peroxide solution. Samples were immerged and stirred in this mixture at room temperature during 5 to 60 seconds. The samples used for the metallographic etching were those used previously to characterize the relative density by the micrographic cross-sections method. Micrographic observations were made with an Alicona InfiniteFocus device, at x10 magnification (pixel size: 0.88 µm).

5.4.2. Electron backscatter diffraction (EBSD)

In order to perform EBSD analyzes, the surface finish of the samples must be perfectly polished, and without damages (scratches, deformations, etc.). For this, an additional OP-S polishing step must be carried out during a minimum of 45 additional minutes, in order to maximize the EBSD image quality [63]. EBSD analyzes were performed on a Zeiss Leo 1530 scanning electron microscope (SEM) equipped with an EBSD detector. The softwares used to analyze EBSD maps were HKL Technology Manager Data and the Matlab toolbox “MTEX” [64,65]. Each EBSD map measures 1.5×1.5 mm square, and the acquisition step-size is 2.5 µm. The disorientation threshold between two grains was set at 15°. The Geometrically Necessary Dislocations (GND) were calculated from the EBSD maps with MTEX, according to [66]. The grain size and aspect ratio (i.e. the ratio of the height to the width of each grain) were calculated with the ImageJ software by fitting an ellipse for each grain, as shown in Figure 10. The ellipses were fitted automatically on the grain boundaries maps using the ImageJ software “Fit ellipse” function. The software fits the “best ellipse” for each grain morphology. The “best ellipse" is drawn according to the barycenter coordinates of the grain (the centroid), its longest and shortest axis. The ellipses have approximately the same areas as the grains they represent. The aspect ratio being calculated by considering the major and minor axes of the ellipses.

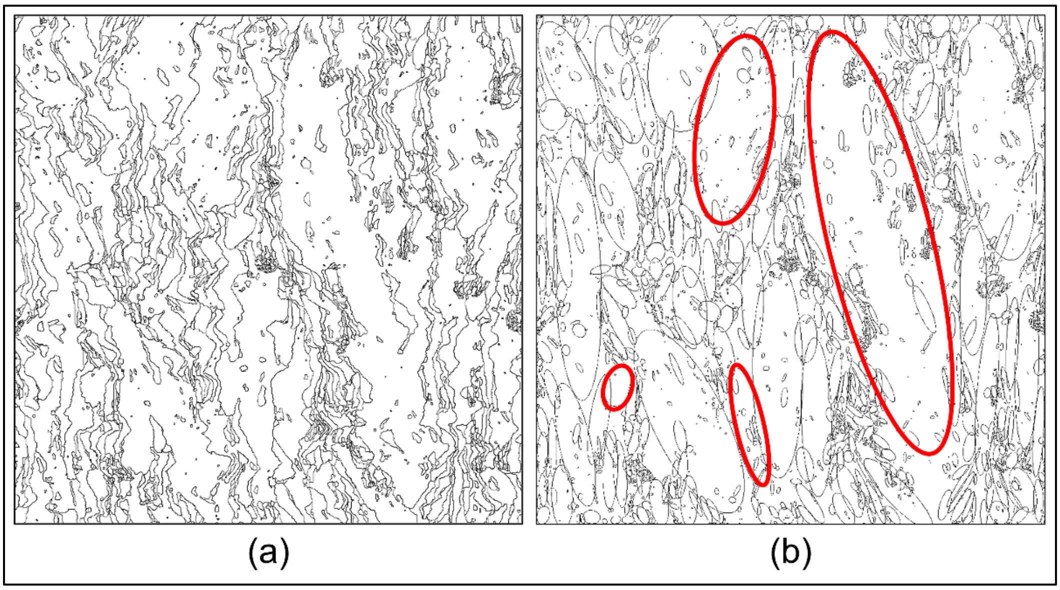

Figure 10 – Example of a grain boundaries map obtained by EBSD via MTEX (a) and the associated fitted ellipses to estimate grain size and aspect ratio obtained via ImageJ® (b).

5.5. Mechanical properties measurements

5.5.1. Tensile properties

The tensile tests were performed under air on dedicated samples (machined according to NF EN ISO 6892-1) on an MTS servo-hydraulic testing machine with a 100 kN load cell at room temperature and at 250 °C. The strain rate was fixed at 2.5×10^{-4} s^{-1}, and the deformation was followed up by an MTS quartz extensometer. Three specimens were tested per process and condition.

5.5.2. Micro hardness

The microhardness measurements were performed on an MMT-X7B Matsuzawa device equipped with a Vickers indenter under a 1 kgf load for 15 seconds. Two samples were characterized along a cross-section parallel to the building direction (BD), and two others along a cross-section perpendicular to BD. Two sections per sample were tested (i.e. 4 horizontal and 4 vertical sections per manufacturing condition), and a matrix of 14 measurements was performed for each section, following the sketch in Figure 11. Results given in this study are an average of all the measurements taken for each condition (either parallel or perpendicular to BD).

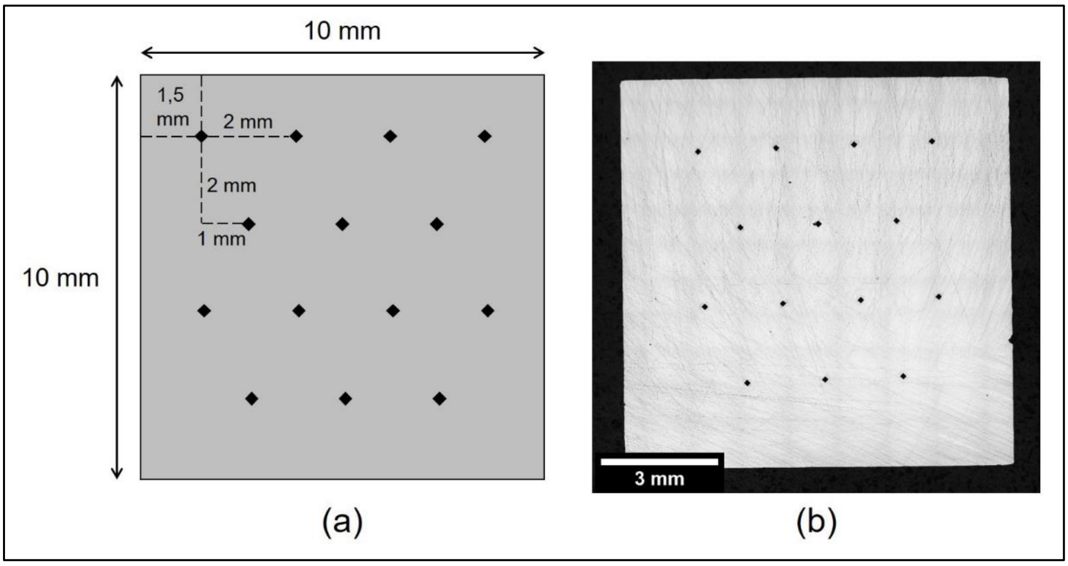

Figure 11 – Schematic illustration of the indentation matrix used (a) and example of cross-section after micro hardness measurements (b).

5.6. Electrical conductivity

The phase-sensitive eddy current method was used to characterize the electrical conductivity (σ) of the samples. Six independent measurements were performed on each sample with a Sigmascope SMP350 device from Fischer, on the top XY horizontal (i.e. perpendicular to BD) polished surface (grade P4000) to reach a Rz roughness value lower than 12 µm. Values are given in MS/m and in % IACS (International Annealed Copper Standard). As already stated in section 3.1, the 100 % IACS electrical conductivity is of 58 MS/m in the international unit system and generally corresponds to the electrical conductivity of an Electrolytic Tough-Pitch copper (Cu-ETP) in annealed state. In this study, the measurements are used as a comparative property as this method is superficial and local.

5.7. Thermal conductivity

The thermal conductivity (K) was calculated according to the following equation (1) [67], with: *K*, the thermal conductivity of the sample (W/(m.K)); *ρ*, the density of the sample (kg/m^3), *Cp*, the specific heat capacity of the sample (J/(kg.K)) and *α*, the thermal diffusivity of the sample (m^2/s).

$$K = \rho \times Cp \times \alpha \qquad \textbf{\textit{(1)}}$$

The real density (ρ) was measured by helium pycnometry (cf. section 5.3.3). The Specific Heat Capacity (Cp) was measured by Differential Scanning Calorimetry (DSC) with a STA449 F1 device from Netzsch, and the thermal diffusivity (α) was measured by the Laser Flash Technique (LFA) with a LFA 457 device, also from Netzsch. In both cases, the temperature ranged from 30 to 450 °C.

Knowing the electrical conductivity (σ), another way to determine the thermal conductivity is to calculate it with the Wiedemann-Franz law (2). This method was used to determinate these values at room temperature (20 °C).

$$K/\sigma = L \times T \qquad \textbf{\textit{(2)}}$$

with: *K*, the thermal conductivity of the sample (W/(m.K)); *σ*, the electrical conductivity (S/m); *L*, the Lorenz number ($L = 2.44 \times 10^{-8}$ W.Ω.K^{-2}); *T* the temperature (K).

6. RESULTS AND DISCUSSION

6.1. Chemical compositions

The results from the chemical composition analyzes are presented in Table 2. It can be noted that the samples produced by EBM exhibit an oxygen level that is twice as low as the samples produced by L-PBF. This can be explained by the fact that the EBM process is carried out under vacuum, unlike L-PBF processes which are carried-out under a protective atmosphere such as argon, nitrogen or helium (with usually a O_2 rate < 1000 ppm), which can lead to a significant oxidation of the material. In addition, other elements such as P, Fe or Si, are present with higher levels in the L-PBF samples as compared to the EBM samples.

Concerning the MFDM process, the level of impurities (C, O) seems to be slightly higher than those measured for the other processes. This trend is probably due to the quality of the powder used and could also be explained by the presence of residual binder inside the part.

Processes	**Elements (wt%)**								
	Cu	*C*	*O*	*S*	*P*	*Fe*	*Sn*	*Si*	*Ti*
EBM	Bal.	0.004 ± 0.001	0.014	0.001	< 0.003	< 0.003	< 0.003	< 0.005	< 0.003
L-PBF high-power infrared laser	Bal.	0.005 ± 0.001	0.031 ± 0.003	< 0.003	< 0.003	0.006 ± 0.004	0.002 ± 0.001	< 0.005	< 0.003
L-PBF green laser	Bal.	0.005 ± 0.001	0.030 ± 0.004	< 0.003	< 0.010	0.002 ± 0.001	< 0.001	0.009 ± 0.001	0.001 ± 0.001
MFDM	Bal.	0.029 ± 0.006	0.022 ± 0.005	< 0.003	< 0.010	0.009 ± 0.003	< 0.001	0.012 ± 0.002	0.001 ± 0.000

Table 2 – Chemical composition (wt%) of the samples manufactured with the different processes.

6.2. Surface roughness

Table 3 below shows the average roughness values measured on three different planes for each manufacturing process (cf. Figure 7). It should be noted that the L-PBF samples produced with a high-power infrared laser were received sandblasted and not in "as-built" state.

Processes	**Surfaces**		**Roughness values (µm)**			
			Ra	*Rz*	*Rp*	*Rv*
EBM As built	Horizontal	XY side	24 ± 2	197 ± 15	126 ± 19	107 ± 12
	Vertical	XZ side	50 ± 4	396 ± 5	222 ± 26	233 ± 16
		YZ side	50 ± 4	378 ± 35	215 ± 53	235 ± 20
L-PBF Infrared high-power laser sandblasted	Horizontal	XY side	6 ± 1	49 ± 6	24 ± 0	46 ± 23
	Vertical	XZ side	10 ± 0	44 ± 4	32 ± 7	33 ± 4
		YZ side	11 ± 2	49 ± 4	28 ± 3	34 ± 1
L-PBF Green laser As built	Horizontal	XY side	13 ± 1	110 ± 5	69 ± 7	64 ± 6
	Vertical	XZ side	20 ± 1	165 ± 11	89 ± 15	105 ± 5

		YZ side	19 ± 1	156 ± 7	83 ± 7	95 ± 6
MFDM As post-treated	Horizontal	XY side	5 ± 0	64 ± 1	40 ± 7	41 ± 5
	Vertical	XZ side	12 ± 0	75 ± 2	38 ± 1	43 ± 1
		YZ side	13 ± 1	88 ± 5	44 ± 0	51 ± 6

Table 3 – Roughness values measured for each additive manufacturing processes studied. The Ra value corresponds to the arithmetical mean of the absolute values of the profile deviations from the mean line of the roughness profile, the Rz value corresponds to the average peak-to-valley height of the roughness profile and the Rp and Rv correspond, respectively, to the maximum peak height of the roughness profile and to the maximum valley depth of the roughness profile. Note that the L-PBF HPIR samples were received in a "sandblasted" condition.

The results obtained for each manufacturing process show that the horizontal surfaces (XY sides) present a roughness significantly lower than the vertical surfaces (YZ and XZ sides).

In additive manufacturing, the roughness of parts resulting from powder bed fusion (PBF) processes (L-PBF, EBM) is linked to three phenomena: (a) the staircase effect, (b) the manufacturing strategies and (c) the agglomeration of powder particles on the surface. The staircase effect comes from the superposition of the layers and is amplified with inclined surfaces and increased layer thickness, as shown by Strano et al. [68] or by Tian et al. [69]. As for manufacturing strategies, various parameters (such as the scan speed, the layer thickness, the hatching distance, the particle size distribution, the use of the skywriting or delay mode, the use of contours, etc.) affect the surface topology, the geometry accuracy and the PBF beads shape, as shown by Tian et al. [69] or Hong et al. [70]. These parameters and strategies directly influence the surface roughness of parts, in addition to the staircase effect. Finally, the powder particles agglomeration is a consequence of the low thermal conductivity of the powder bed. At the part/powder interfaces (i.e. the part surfaces), the temperature is higher than inside the part. This tends to partially melt powder at those interfaces and to attach them to the part surfaces, leading to an agglomeration of powder particles, as it can be evidenced by Tian et al. [69]. This explains the higher values in the vertical planes (i.e. along the building direction), and also the higher values for the EBM process (higher layer thicknesses and particles size distribution, cf. section 2.2) compared to the L-PBF process with a green laser.

The sandblasting finishing step of the L-PBF samples manufactured with an infrared high-power laser explains the lower roughness values, although vertical surfaces always have higher values than horizontal surfaces. Interestingly, the sandblasting step performed by the manufacturer was not able to homogenize the roughness between the vertical and horizontal faces.

In the case of the MFDM process, roughness is particularly associated with the "staircase effect" (superposition of layers). Since the material is not built inside a powder bed the phenomenon of agglomeration of powder particles on the surface does not exist, which tends to reduce the roughness of the parts. In the case of the MFDM process, the size of the extrusion nozzle controls the diameter of the strands deposited, which influences the surface topology of the parts (undulation) more than the roughness.

In the literature, various authors have already presented roughness values comparable to the results obtained in this study. For example, in the case of the EBM process, Wang et al. [71] show Ra values ranging from 24 µm to 41 µm on verticals sides and from 20 µm to 34 µm on horizontals sides, on a TA6V alloy. In the case of the L-PBF process, Constantin et al. [1] show a Ra value of 18 µm on pure copper, whereas Bonesso et al. [39] measured on lateral surfaces Ra from 11.7 µm to 2.9 µm, depending on the powder Particle Size Distribution and SPAN index. Rodriguez et al. [57] measured a Ra value of 3.3 µm, a Rz value of 18.5 µm and a Rmax value of 23.9 µm on the XY side (i.e. horizontal surface) on samples manufactured with the Atomic Diffusion Additive Manufacturing technology, which is similar to the MFDM process.

6.3. Density

6.3.1. The Archimedes' method measurements

The relative density and the “open porosity” rate of each process were characterized with the Archimedes’ method using anhydrous ethanol. The results are given in the Table 4.

	Processes			
	EBM	*L-PBF infrared high-power laser*	*L-PBF green laser*	*MFDM*
Relative density (%)	99.1 ± 0.1	99	99.1 ± 0.1	98.8 ± 0.3
“Open porosity” rate (%)	1.1 ± 0.2	0.1	0.9 ± 0.2	8.2 ± 5.7

Table 4 – Relative density and “open porosity” rate results of samples manufactured with each process and measured with the Archimedes’ method.

The relative densities measured with this method do not consider the "open porosity” because the measuring fluid fills them during the second weighing (immersion step).

In the case of this study, and for the samples manufactured with the "direct" processes, the "open porosity” rates are associated to the surface roughness of the samples more than to real lack of fusion opening towards the surface of the samples. Indeed, in the case of the EBM process, the Rv values (cf. Table 3) are the highest (234 µm) as is the “open porosity” rate (1.1 %). Conversely, the sandblasted samples (infrared high-power laser L-PBF) whose Rv values are the lowest (34 µm), present the lowest “open porosity” rate too (0.1 %). Finally, in the case of the L-PBF samples manufactured with a green laser, the Rv values are intermediate (100 µm), as is the “open porosity” rate (0.9 %).

It can be noted that the MFDM process exhibits a very high “open porosity” rate unlike the powder bed processes (EBM, L-PBF). This can be explained by the fact that there is no material (powder) between the strands of material deposited horizontally and vertically. This “void” or absence of material between the strands can be connected to the external surface of the part. During sintering, these empty spaces remain as they are, leading to the presence of open porosities in the MFDM parts. This “open porosity” rate is an important data to measure in post additive manufacturing characterizations. Indeed, although the relative density is high, it does not take into account the “open porosity”, which can falsify the interpretation of the results of other analyzes (relative density, mechanical properties).

6.3.2. The micrographic cross-sections measurements

To correlate the relative density measured with the Archimedes' method, and in order to characterize the porosities (type, size, and location), micrographic cross-sections were analyzed on the samples used previously. The Figure 12 illustrates the cross-sections for each manufacturing process, and Figure 13 shows examples of typical porosities according to each of the manufacturing process used. The relative density results measured for each process are given in Table 5.

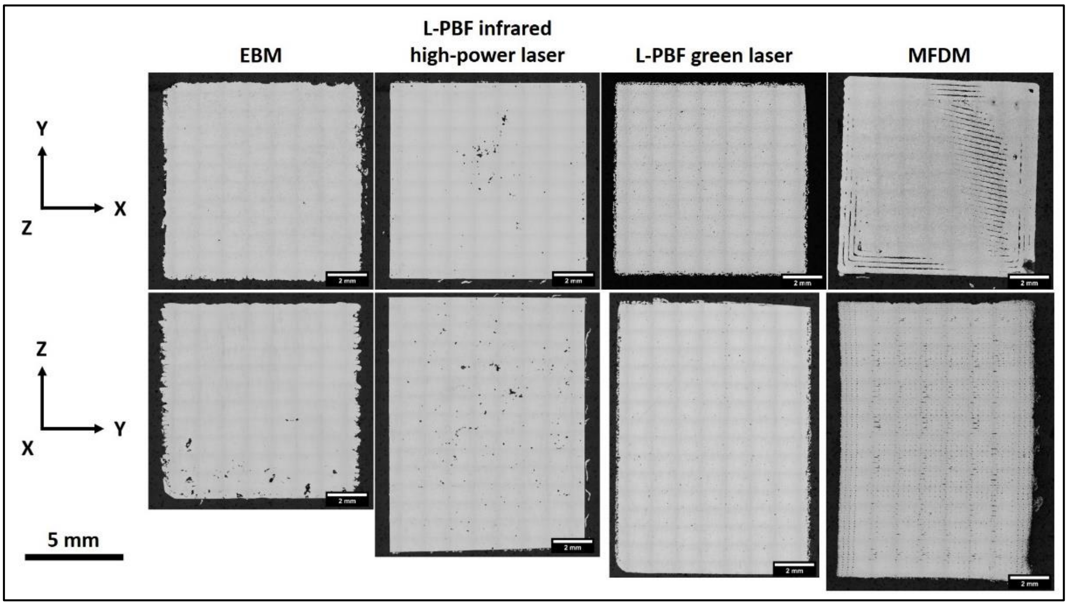

Figure 12 – Micrographic cross-sections of samples from each additive manufacturing process. The relative density associated to these micrographic cross-sections are respectively: 99.9 % (EBM), 99.7 % (L-PBF infrared high-power laser), 99.7 % (L-PBF green laser) and 96.9 % (MFDM).

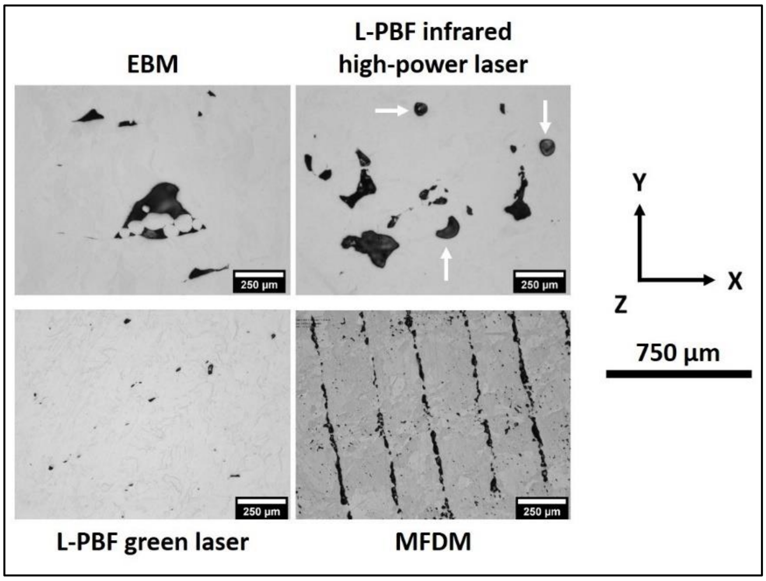

Figure 13 – Micrographic details of typical porosities inside Cu samples obtained from each additive manufacturing process. It can be observed that, in the case of samples manufactured with the L-PBF infrared high-power laser, two different types of porosities are observed: lack of fusion and keyholes (white arrows).

	Processes			
	EBM	*L-PBF infrared high-power laser*	*L-PBF green laser*	*MFDM*
Relative density (%)	99.6 ± 0.3	99.7 ± 0.1	99.8 ± 0.1	98. ± 0.9

Table 5 – Relative density results of samples manufactured with each process and measured with the micrographic cross-sections analysis method.

The tendency obtained with the micrographic cross-sections analyses are comparable to those obtained with the Archimedes' method (cf. Table 4). The L-PBF process using a green laser produces the densest parts, followed by the EBM and the infrared high-power laser L-PBF processes (which both give similar results). It should be noted that, in the case of samples manufactured with the "direct" processes, the micrographic cross-sections method gives results systematically higher than those obtained with the Archimedes' method. This phenomenon has already been observed and discussed, and the most probable explanation given by De Terris et al. [61] is that a porosity section is not representative of its volume, due to its very irregular shape in AM (and particularly in the case of lack of fusion). In addition, it is possible that despite all the care taken during the preparation of the samples (polishing steps), some porosities were masked because of the "buttering" effect of the polished and analyzed surface.

Moreover, Figure 13 reveals that, in the case of the “direct” processes, the main porosity type is assimilated to a lack of fusion (LOF). Porosities are mainly irregularly shaped and can contain un-melted powder particles. These LOF reflect a too low energy input brought to the material, which does not allow a sufficient melting of the powder layer. The parts therefore have areas that have not been properly melted, and which are characterized as being porosities of the “lack of fusion” (LOF) type.

In the case of the EBM process, these porosities are localized at the bottom of the parts (Figure 14). One explanation would be that the optimum thermal conditions for melting the powder bed are not reached at the start of the EBM process, but are only reached after a certain manufacturing time. In the case of the L-PBF process using a high-power infrared laser, these LOFs are distributed randomly, which can be explained by a local and temporary decrease in the energy density brought to the material during the process. This random decrease in energy density has many origins, such as the high reflectivity of the material, a partial absorption of the laser beam by the vapor plume generated during the process, or even by the presence of ejections laid on the powder bed preventing the powder located below from melting. It should be noted that this process also exhibits occluded gas porosities (Figure 13), associated to the keyhole regime. This regime occurs at high laser intensity I (order of magnitude : $I > 10^6$ W/cm²) and leads to the metal vaporization and the occurrence of gas porosities, as explained by King et al. [72] or by Jadhav et al. [28]. Finally, in the case of the L-PBF process using a green laser, the porosities seem aligned along the scan paths on the XY plane (Figure 14), which reflects a slightly too high hatch-spacing, which does not allow a good mutual lateral covering of the beads.

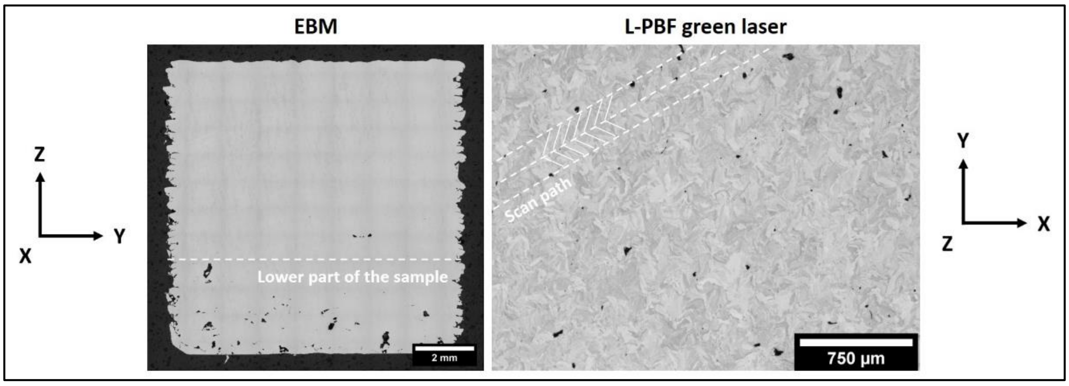

Figure 14 – Localization of the porosities in samples manufactured with the EBM process and the L-PBF process using a green laser.

Figure 12 and Figure 13 show that in the case of the MFDM process, porosity is mainly a consequence of a too large hatching distance between the deposited strands. This could be easily solved by reducing this hatching distance during the definition of the process parameters.

Various authors have studied the density of pure copper parts manufactured by additive manufacturing, using micrographic cross sections analyses. For example, Raab et al. [73] show that using the EBM process, it is possible to manufacture samples denser than 99.95 %. Guschlbauer et al. [17] report a density higher than 99.5 %, as in our study. About the L-PBF process, the use of a high-power infrared laser allows Colopi et al. [29] to manufacture samples with a density of 99.1 %, whereas the use of a green laser allows Gruber et al. [32] to reach a density of 99.99 %. Finally, (using the Archimedes' method) Singh et al. [10] show a sintered sample with a density of 94.5 % which was manufactured with a process comparable to the MFDM process. Rodriguez et al. [57] measured a relative density (using the Archimedes' method too) around 94.5 % on samples manufactured with the Atomic Diffusion Additive Manufacturing (ADAM) technology (MFDM-like process). Canadilla et al. [74] have manufactured samples using Material Extrusion Additive Manufacturing (again a MFDM-like process) which exhibit a relative density of 95.3 % ± 0.5 (using the Archimedes' method too).

6.3.3. The helium pycometry measurements

The Table 6 shows the density at room temperature (20 °C) of the samples used to measure the thermal conductivity (cf. section 5.7 and section 6.7.2). As done in section 4.3.1, the relative density of the samples was calculated considering that the theoretical pure copper density is 8.96 g/cm^3.

Processes	*EBM*	*L-PBF high-power infrared laser*	*L-PBF green laser*	*MFDM*
Real density (g/cm^3)	8.903	8.874	8.889	8.876
Relative density (%)	99.4	99	99.2	99.1

Table 6 – Density results at room temperature (20 °C) of the samples manufactured with each process and measured with the helium pycnometry method. These values are considered in the calculation of the thermal conductivity (cf. equation (1)).

First of all, it can be seen that the relative density calculated in this section are very similar to the results obtained from the Archimedes' method (cf. Table 4 : EBM = 99.09 % ; L-PBF-HPIR = 99.03 % ; L-PBF-GL = 99.14 % ; MFDM = 98.82 %). This tends to validate the Archimedes' method as a relevant, simple and fast way to estimate the relative density of AM parts. Moreover, it appears that the relative density of the MFDM sample seems to be overestimated, as in the Archimedes' method results. This can be explained by the use of helium instead of ethanol, based on [61]. The He atom being smaller than the ethanol molecule, it can penetrate deeper inside the "open porosities" of this sample, leading to a more precise measurement of all the volume of the sample (including the closed porosities). It seems important to mention here that the real density of the samples is related to their chemical composition too. As it can be seen in Table 2, the samples are not composed of pure copper only and elements such as C, O, Fe or Si could influence the real density measured value (leading to the difference highlighted in the relative density result).

6.4. Microstructures

6.4.1. Micrographic cross-sections analyzes using a chemical reagent

The use of a chemical reagent reveals columnar grains along the building direction (XZ plane) and apparently-equiaxed grains in the XY plane in the case of the samples manufactured with the "direct" processes (Figure 15). This observation is common in additive manufacturing involving the melting of the metal: the material solidifies according to the thermal gradient (that is mainly along the building direction) and the grains germinate by epitaxy on the previous ones, as indicted by [75] in the case of the welding metallurgy. Micrographic cross sections in the XY plan reveal the scan paths too. These observations are similar to those made by [17] for the EBM process, and by [32] for the L-PBF process using a green laser. Concerning the MFDM process, the Figure 15 shows that the microstructure is equiaxed in the XY and XZ planes. During the manufacturing process, the samples are densified by sintering at high temperature (close to the copper melting point). The densification occurs in several steps: first, the welding of the powder grain between them; then, the grain growth associated with the removal of the open porosity and the closed porosity. At high temperature, the mechanisms of sintering are mainly the volume diffusion and also the diffusion at grain boundaries.

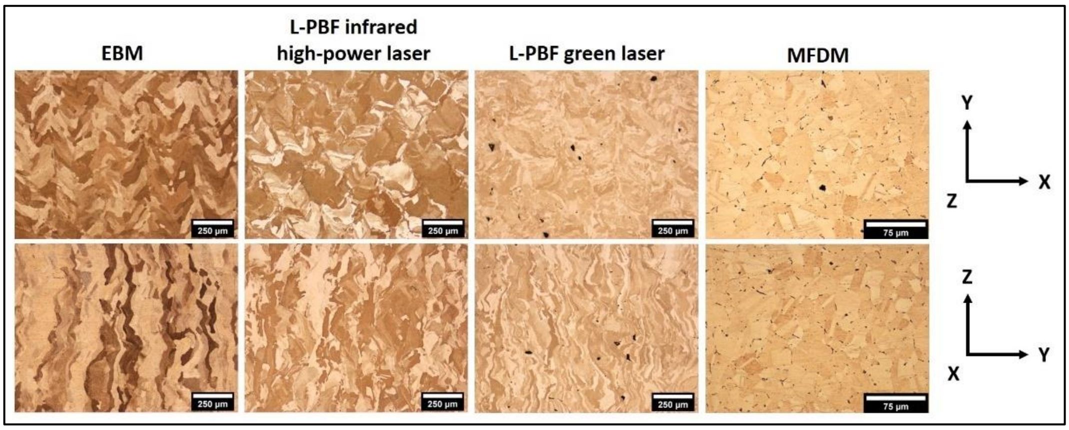

Figure 15 – Micrographic cross sections of the samples after being etched with a chemical reagent.

6.4.2. EBSD characterizations

The EBSD analyzes of the various samples reveal microstructures which are comparable to those observed by optical micrographs after an attack with a chemical reagent (Figure 16). However, EBSD analyzes allow also the calculation and comparison of grain sizes, as well as the calculation of GND density for each sample. These results are given in Table 7. The samples manufactured by the L-PBF processes exhibit the highest GND densities, followed by the samples manufactured by the EBM process. This is explained by the highest cooling rate involved in the L-PBF process (10^5 to 10^7 K/s) compared to the EBM process (10^3 to 10^5 K/s), and by the fact that the EBM process is carried out at high temperature (the powder bed being heated at 500-600 °C), which lead to a partial dynamic annealing. The calculated GND densities of the L-PBF processes are similar to the values obtained on an Inconel 625 superalloy, as shown by [66].

Moreover, it can be observed that the EBM process generates samples with a higher grain size (around two times bigger) in both XY and XZ planes, compared to the L-PBF processes. This is induced by the lower cooling rate involved in the EBM process. In the case of L-PBF processes, it appears that the use of a high-power infrared laser induces bigger grains than the use of a green laser. This can be explained by the fact that as the infrared absorption is lower than the green absorption, therefore it requires a high laser power to correctly melt the powder bed in infrared conditions. This higher power induces a global warmer sample, reducing the average thermal gradient. This manufacturing condition can also explain the lower GND density of the samples manufactured with the high-power infrared laser compared to the samples manufactured with a green laser.

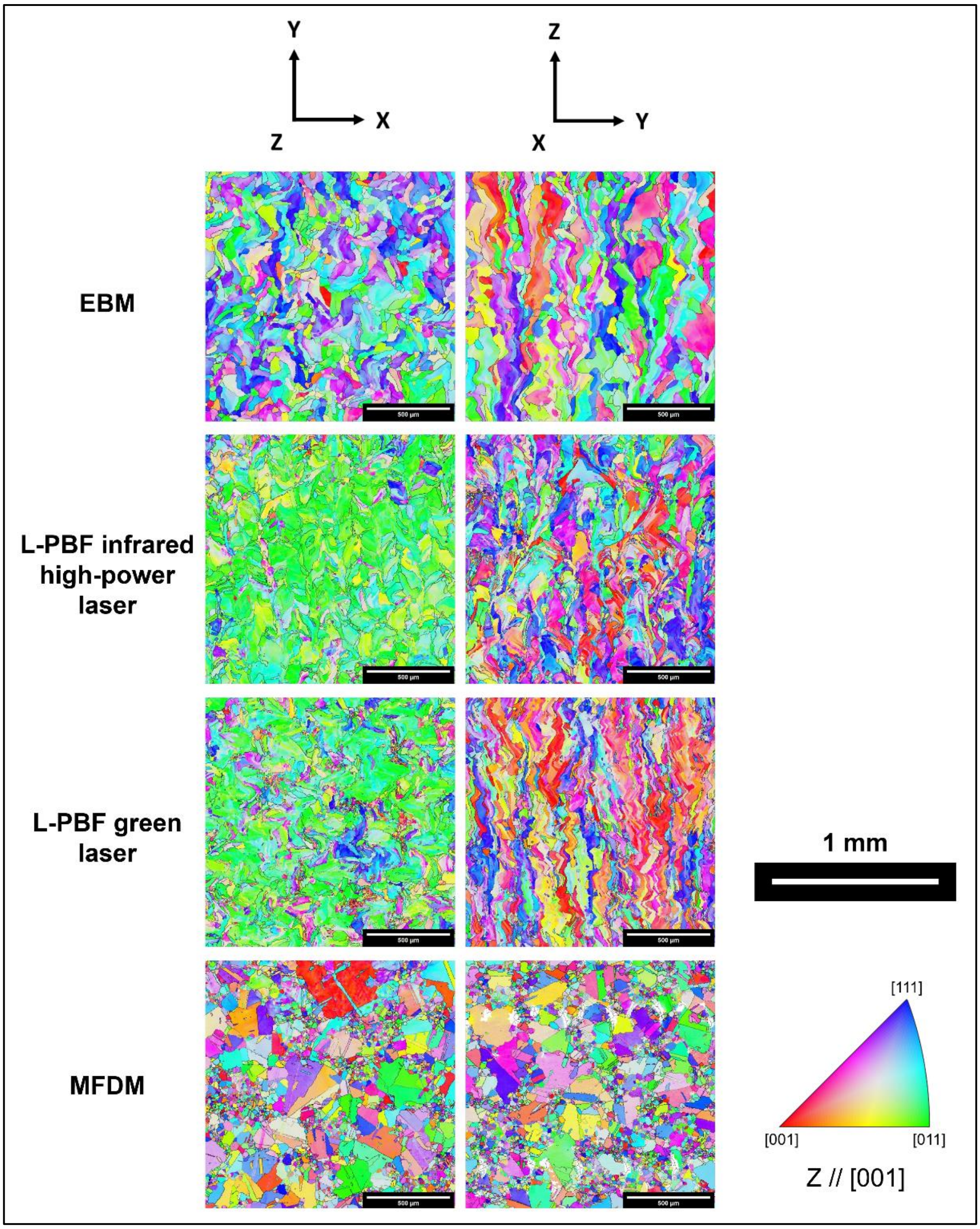

Figure 16 – EBSD maps of the XY cross-section (i.e. perpendicular to the building direction Z) and YZ cross-section (i.e. parallel to the building direction Z) of the different samples. The scale bar of each EBSD maps represents 500 µm.

Processes	**Sections**	**GND density (10^{15} m/m^{3})**	**Equivalent diameter (µm)**			**Aspect ratio**		
			Max.	*Average*	*Median*	*Max.*	*Average*	*Median*
EBM	*XY*	1.40	291	35 ± 35	25	13	2 ± 1	2
	XZ	1.28	478	38 ± 49	22	19	3 ± 2	2
L-PBF high-power infrared laser	*XY*	2.88	330	20 ± 29	9	12	3 ± 1	2
	XZ	2.44	271	15 ± 25	6	17	3 ± 2	2
L-PBF green laser	*XY*	3.33	530	12 ± 23	6	20	2 ± 1	2
	XZ	2.75	632	13 ± 27	5	14	3 ± 2	2
MFDM	*XY*	0.67	261	13 ± 18	8	25	2 ± 1	2
	XZ	0.52	224	11 ± 15	7	23	2 ± 1	2

Table 7 – GND densities and grain sizes calculated from the EDSD analyses for each manufacturing processes.

6.5. Mechanical properties

6.5.1. Tensile tests results

Tensile tests were carried out on specimens produced according to the various processes described in this study. A first series of tests was carried out at room temperature, while a second series of tests was carried out at 250 °C. In both cases, samples manufactured along the building direction (BD) and inclined at 45° with respect to BD (Table 1), were tested. Results are given in Table 8. It has to be noted that the L-PBF process using an infrared high-power laser produced horizontal samples instead of 45° samples. Moreover, some specimens were broken during machining which did not allow several tests to be carried out under certain conditions (L-PBF using a green laser at 250 °C with an 45° orientation, or MFDM samples at 250 °C with a vertical orientation).

Processes	**Temperature (°C)**	**Orientation**	**$Rp_{0.2}$ (MPa)**	**Rm (MPa)**	**A%**
EBM	*20*	*45°*	92 ± 5	173 ± 7	38 ± 12
		Vertical	99 ± 1	210 ± 5	37 ± 2
	250	*45°*	68 ± 0	110 ± 4	27 ± 8
		Vertical	71 ± 3	117 ± 2	16 ± 2
L-PBF high-power infrared laser	*20*	*Horizontal*	152 ± 3	214 ± 3	38 ± 3
		Vertical	146 ± 3	203 ± 4	39 ± 13
	250	*Horizontal*	113 ± 2	132 ± 2	17 ± 2
		Vertical	113 ± 2	133 ± 3	22 ± 5
L-PBF green laser	*20*	*45°*	144 ± 5	198 ± 6	47 ± 9
		Vertical	146 ± 1	205 ± 3	51 ± 6
	250	*45°*	116	124	25
		Vertical	116 ± 1	130 ± 2	30 ± 0
MFDM	*20*	*45°*	102 ± 44	159 ± 45	22 ± 21
		Vertical	78 ± 28	149 ± 27	12 ± 4
	250	*45°*	47 ± 4	98 ± 25	11 ± 6
		Vertical	62	110	14

Table 8 – Tensile properties of pure copper at room temperature and 250 °C and manufactured with different additive manufacturing processes.

As could have been a priori expected, the tensile tests results show that the mechanical properties are higher in the case of the "direct" processes. This can be explained by the melting of the powder which create a new material at the solidification. Moreover, the higher porosity rate in the MFDM process combined with a lower metallurgical bonding between powder particles explain the poor tensile properties of this process.

The EBM process exhibits a lower yield strength in each test condition, compared to the L-PBF processes which both exhibit higher and comparable $Rp_{0.2}$ values. This could a priori be explained by the fact that the EBM samples seem to be more ductile (the GND density and hardness values (cf. Table 7) are lower) than the L-PBF samples, due to a high temperature manufacturing process which acts like a dynamic stress relieve heat treatment. However, this observation is not in adequation with the elongation trend: the A% values should be higher in the case of the EBM process whereas it is not the case. This could be due to variation in dislocation density between the processes.

At 250 °C, the tensile properties decrease for all the processes, although the general trend observed at room temperature remains the same.

Compared to the literature results, in this study the EBM values are higher than those of Guschlbauer et al. [17] (vertical orientation: Yield Strength = 78 MPa ; Tensile Strength = 177 MPa ; A% = 59 %, and 45° orientation: Yield Strength = 87 MPa ; Tensile Strength = 158 MPa ; A% = 14 %). The L-PBF process using a green laser gives values which are higher than those of Gruber et al. [32] too (vertical orientation: Yield Strength = 136 MPa ; Tensile Strength = 212 MPa ; A% = 52 %, and 45° orientation: Yield Strength = 127 MPa ; Tensile Strength = 188 MPa ; A% = 47 %). However, using a medium power infrared laser (P < 500 W), Jadhav et al. [28] measured tensile properties similar to those of this study in an horizontal orientation (Yield Strength= 122 MPa ; Tensile Strength = 211 MPa ; A% = 43 %). Using a MDFM-like process, Rodriguez et al. [57] or Canadilla et al. [74] measured respectively the follow tensile properties on horizontal samples: Yield Strength = 45.7 MPa ; Tensile Strength = 205.9 MPa ; A% = 37 % and Yield Strength = 65 MPa ; Tensile Strength = 205.8 MPa ; A% = 35.1 %, Canadilla's results appearing to be significantly better than ours.

6.5.2. Micro hardness measurements

Micro hardness tests were performed as described in section 5.5.2. The average results are given in the Table 9 below.

	Cross sections	EBM	L-PBF high-power infrared laser	L-PBF green laser	MFDM
Micro hardness (HV_1)	*Horizontal*	50 ± 2	69 ± 2	67 ± 1	47 ± 3
	Vertical	50 ± 2	66 ± 2	66 ± 2	43 ± 1

Table 9 – Micro hardness of pure copper samples manufactured according to the different AM processes studied.

The L-PBF processes exhibit the higher hardness values compared to the EBM process. This manifests a lower ductility of pure copper additively manufactured by the L-PBF processes. This is in adequation with the higher GND density measurements and lower grain size determination (cf. Table 7) and tensile properties (cf. Table 8). It has to be noted that no major differences are observed according to the orientation of the cross-section, although the grain size varies depending on the cross-section orientation. It can be observed that the MFDM samples show a lower micro hardness which can be explained by a low adhesion between the sintered powder particles, as it can be highlighted int the Figure 17 where a decohesion of the particles is visible around the indent. This is in adequation with Ternero et al. [76] who show that the hardness of sintered samples decreases as the porosity increases.

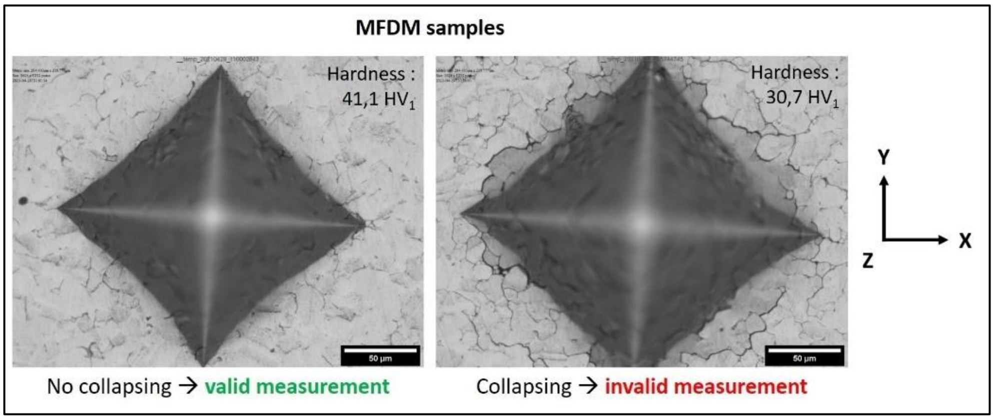

Figure 17 – Visualization of the decohesion and collapse of the sintered powder particles which can be observed in some MFDM samples.

In the literature, Guschlbauer et al. [17] measured a micro hardness comprised between 55.5 to 57.8 $HV_{0.05}$ for samples manufactured with the EBM process along the building direction, which is slightly higher than our measurements. Jadhav et al. [28] measured a micro hardness of 66 $HV_{0.03}$ on samples manufactured by L-PBF using a medium power ($P < 500$ W). Rodriguez et al. [57] measured a micro hardness value of 37.6 HV_1 on samples manufactured with the Atomic Diffusion Additive Manufacturing (ADAM) technology (i.e. MFDM-like process) whereas Canadilla et al. [74] measured a micro hardness of 54.8 $HV_{0.05}$ ± 2.1 using a similar indirect process.

6.6. Electrical conductivity

The results of the electrical conductivity measurements are given in Table 10, for each manufacturing process. The values reported represent an average of 18 measurements carried out on 3 different samples per process (6 measurements per sample). Note that due to the method used to determine the electrical conductivity of the samples, these results are considered as superficial and local.

	Electrical conductivity (MS/m)	
Processes	*MS/m*	*% IACS*
EBM	58.8 ± 0.2	101
L-PBF infrared high-power laser	57.6 ± 0.3	99
L-PBF green laser	58.0 ± 0.1	100
MFDM	51.2 ± 1.5	88

Table 10 – Electrical conductivity measured for each process.

It should be noted that the electrical conductivity of the test samples mainly depends on three factors (the influence of the temperature is not considered here), which in the case of this study vary between each sample produced (depending on the process). This complicates the discrimination of the effect of each factor on this property and thus to identify the influence of the process on the electrical conductivity:

- the *chemical purity* of the copper, as shown by Chapman [77],
- the *mesostructured* of the material and the existence of *sintering neck* that reduce the electron flow (in the case of MFDM process), as shown by Yegyan Kumar et al. [21] on pure copper samples manufactured by Metal Binder Jetting (MBJ) process,

- the *residual stress rate* of the material (or plastic deformation)*,* as shown by Çetinarslan [78] (characterized in this study by the dislocation density GND or the micro-hardness measurements).

It emerges from this analysis that the samples exhibiting the highest electrical conductivity are the samples manufactured with the "direct" processes. Indeed, the direct-manufacturing processes offering much denser samples (Table 4, Table 5, Table 6), which explains the major difference in electrical conductivity. As the relative density decreases (helium pycnometry measurements: EBM = 99.36 % ; L-PBF-Green laser = 99.21 % ; L-PBF-High power infrared laser = 99.04 %), as the electrical conductivity decreases too (Table 10).

Moreover, in this study, the EBM process presents the samples with the purest chemical composition (cf. Table 2), and the highest electrical conductivity. In addition, the EBSD analyzes (via the calculation of the GND densities), show that the samples produced by EBM exhibit a less dislocated microstructure than the samples produced by L-PBF (cf. Table 7). This observation is reinforced through the hardness measurements; the EBM samples exhibit lower micro hardness values than the L-PBF samples (Table 9). Finally, the average grain size (equivalent diameter) resulting from the EBSD analysis (Table 7) shows that the EBM process induces larger grains (i.e. lower grains boundaries), which is favorable in term of electrical conductivity.

In the literature, Guschlbauer et al. [17] show that samples manufactured with the EBM process have a maximal electrical conductivity of 59.1 MS/m (i.e. 101.9 % IACS), which is slightly higher than our study. Concerning the L-PBF processes, using a medium-power infrared laser (P < 500 W), Jadhav et al. [28] have manufactured samples with an electrical conductivity of 54.5 MS/m (i.e. 94 % IACS). Using a high-power infrared laser (> 500 W) Jadhav et al. [30] have produced parts with an electrical conductivity ranging from 48,1 to 51.0 MS/m (i.e. 83 to 88 % IACS), which is lower than the results of this study, using a high-power IR laser. Using a green laser, Gruber et al. [32], have manufactured samples with an electrical conductivity from 57.3 to 58.1 MS/m (i.e. 98.6 to 100 % IACS), which is equivalent to the results of this study. Finally, Rodriguez et al. [57] measured an electrical conductivity around 49.5 MS/m (i.e. 86.1 ± 7 % IACS) on samples manufactured with the ADAM technology (i.e. MFDM process), in the same range of our results.

6.7. Thermal conductivity

6.7.1. At room temperature

The thermal conductivity can be calculated with the Wiedemann-Franz law (2) from the previously presented electrical conductivity data. Table 11 reports all the data measured to calculate the thermal conductivity of each sample according to the manufacturing processes. The L and T values being constant, the thermal conductivity K at room temperature follows the same trend as the electrical conductivity σ: the EBM process offers the best result, followed by the L-PBF processes. Again, this could be explained by its lower dislocation density and porosity rate (about the EBM process, the porosities are located at the bottom of the part, and not in the area where the samples were taken). Moreover, the chemical composition could influence these results, as the EBM samples appear to be purest than the other (cf. Table 2).

Processes	**σ (MS/m)**	**L (W.Ω.K^{-2})**	**T (K)**	**K (W/(m.K))**
EBM	58.8	2.44×10^{-8}	293.15	421
L-PBF high-power infrared laser	57.6			412
L-PBF green laser	58			415
MFDM	51.2			366

Table 11 – Thermal conductivity at room temperature of the samples manufactured with different processes.

Guschlbauer et al. [17] report a maximal thermal conductivity of 411.9 W/(m.K) in their study on the additive manufacturing of pure copper by EBM, which is lower than our results. Using a medium-power infrared laser (P < 500 W), Jadhav et al. [28] calculated a thermal conductivity of 392 W/(m.K) from the Wiedemann-Franz law using a Lorenz number (L) of 2.41×10^{-8} WΩK^{-2}. Interestingly, even with the a priori correct value of 2.44×10^{-8} WΩK^{-2} their result would remain below ours. Using a high-power infrared laser (> 500 W) Jadhav et al. [30] have produced parts with an estimated thermal conductivity ranging from 317 to 336 W/(m.K), which is significantly lower than our measurements. From the electrical conductivity measurements of Gruber et al. [32], it is also possible to estimate thermal conductivity of L-PBF samples manufactured with a green laser using the Wiedemann-Franz law: 410 to 416 W/(m.K), which is close to our results. Finally, Canadilla et al. [74] measured a thermal conductivity of 363 W/(m.K) using the laser flash analysis method, again close to our result.

6.7.2. At high temperature

At high temperatures, the thermal conductivity was calculated according to the equation (1) (cf. section 5.7) and the values given in Table 12. The results obtained for different elevated temperatures are given in Table 13. The thermal conductivity values at 20 °C calculated previously are also indicated, as well as the values estimated empirically by linear regression.

Processes	ρ (kg/m^3)	α (m^2/s)				Cp (J/(kg.K))			
	20 °C	*100 °C*	*200 °C*	*300 °C*	400 °C	*100 °C*	*200 °C*	*300 °C*	400 °C
EBM	8903	109.10^{-6}	105.10^{-6}	100.10^{-6}	97.10^{-6}	421	425	428	433
L-PBF high-power infrared laser	8874	107.10^{-6}	102.10^{-6}	98.10^{-6}	95.10^{-6}	421	424	427	432
L-PBF green laser	8889	104.10^{-6}	98.10^{-6}	93.10^{-6}	90.10^{-6}	439	442	443	443
MFDM	8876	91.10^{-6}	88.10^{-6}	83.10^{-6}	80.10^{-6}	435	436	436	440

Table 12 – Average of the measured values of density (ρ, helium pycnometry), thermal diffusivity (α) and specific heat capacity (Cp) used to calculate the thermal conductivity (K) at various temperatures.

Processes	**Thermal conductivity K (W/(m.K))**					
	20 °C (Wiedemann-Franz law)	*20 °C (linear regression)*	*100 °C*	*200 °C*	*300 °C*	*400 °C*
EBM	421	416	407 ± 13	396 ± 16	382 ± 17	374 ± 17
L-PBF high-power infrared laser	412	406	398 ± 13	384 ± 12	372 ± 13	363 ± 15
L-PBF green laser	415	419	406 ± 6	385 ± 6	365 ± 8	353 ± 7
MFDM	366	362	351 ± 31	339 ± 30	322 ± 33	312 ± 33

Table 13 – Thermal conductivity of samples manufactured with different processes, at 100 °C, 200 °C, 300 °C and 400 °C. Values at 20 °C calculated with the Wiedemann-Franz law and estimated with a linear regression are given too.

It is observed that the thermal conductivity drops linearly as the temperature of the samples increases. At high temperatures, the EBM process gives higher thermal conductivities than the L-PBF processes, as at room temperature. A calculation of the thermal conductivity at 20 °C can therefore be made by linear regression. We notice that the results obtained in this way are close to those calculated with the Wiedemann-Franz law. This observation makes it possible to estimate the electrical conductivity of samples at high temperature.

7. CONCLUSION

This study aimed to compare the properties of pure copper parts produced using four different additive manufacturing processes: (1) the Electron Beam Melting process, (2, 3) the Laser-Powder Bed Fusion process, using a high-power infrared laser (HP-LPBF) or a green laser (G-LPBF) and (4) the Metal Fused Deposition Modeling process. The main conclusions drawn from this study are therefore:

- The “direct” processes allow to produce the densest parts (>99 %). No major differences in densities were observed between these processes, excepted that in the case of the EBM process the porosities seem to be located at the bottom of the parts, unlike int the case of the L-PBF processes where they seem to be distributed homogeneously inside the parts. In the case of the MFDM process, due to the void between the deposited strands, the porosity rate is higher.

- The surface roughness of the EBM parts (Ra ~ 50 µm) is higher compared to the L-PBF process (Ra ~ 10 to 20 µm). This comes from the use of a powder which likely exhibits a higher particle size, and the use of layers thicker than in the L-PBF process.
- The micro-hardness measurements of the L-PBF samples are equivalent (> 65 HV_1), regardless of the type of laser used, and are higher than the micro-hardness of the EBM samples (50 HV_1). The MFDM process shows the lower micro-hardness properties compared to the other processes (~ 45 HV_1).
- At room temperature, the tensile test properties show that the EBM samples have a lower yield strength and elongation at break than the L-PBF processes which are similar. However, the ultimate tensile strength of the EBM and L-PBF samples are equivalent. The MFDM samples exhibit the lower tensile properties due to their high porosity rate. At 250 °C, this trend remains the same, although the tensile properties decrease.
- The electrical properties of the samples manufactured with the “direct” processes are higher than those of the “undirect” process. This is possibly due to the lower porosity rate and a higher copper purity. Concerning the “direct” processes, the EBM process is slightly better than the L-PBF process using a green laser, which is better than the one using a high-power infrared laser.
- The thermal properties of the samples manufactured with the EBM process are higher than those of the samples manufactured with the L-PBF or MFDM processes. This can be explained both by the chemical composition of the samples which vary according to the different suppliers, and the material properties (porosities, dislocation densities).
- Finally, our results are in good agreement with those currently available in the scientific literature or given by manufacturers, which confirms that the manufacturers who produced our parts master their processes.

ACKNOWLEDGMENTS AND FUNDING SOURCE

The authors gratefully acknowledge CEA-LITEN and the CEA “Programme Transverse de Compétences” for their financial support with the “ICARE” project. The SEM measurements were performed at the CEA NanoCharacterization Platform (PFNC) - Minatec, supported by the French RTB (IRT Nanoelec) and the equipex NanoIDT. The authors also gratefully thanks J.P. Garandet for his help in improving the presentation of the manuscript, and T. Germain, P. Faucherand, C. Mollard, J. Leforestier and C. Flament for their technical help in this work.

AUTHORS CONTRIBUTION

Thibaut de Terris: Conceptualization, Formal analysis, Methodology, Investigation, Data curation, Software, Writing - original draft, Writing – review & editing. **Céline Ribière:** Investigation, Writing - review & editing. **Thierry Baffie:** Supervision, Formal analysis, Resources, Writing - review & editing.

DECLARATION OF COMPETING INTEREST

The authors declare that they have no known competing financial interests or personal relationships that could have appeared to influence the work reported in this paper.

BIBLIOGRAPHY

[1] Constantin L, Wu Z, Li N, Fan L, Silvain J-F and Lu Y F 2020 Laser 3D printing of complex copper structures *Additive Manufacturing* **35** 101268

[2] Sciacca G, Sinico M, Cogo G, Bigolaro D, Pepato A and Esposito J 2022 Experimental and numerical characterization of pure copper heat sinks produced by laser powder bed fusion *Materials & Design* **214** 110415

[3] Favero G, Bonesso M, Rebesan P, Dima R, Pepato A and Mancin S 2021 Additive manufacturing for thermal management applications: from experimental results to numerical modeling *International Journal of Thermofluids* **10** 100091

[4] Johnson K, Burden E, Shaffer M, Noack T, Mueller M, Walker J, MacDonald E, Cortes P and Quintana J 2022 A copper pyramidal fractal antenna fabricated with green-laser powder bed fusion *Prog Addit Manuf*

[5] Queral V, Rincón E, Cabrera S and Lumsdaine A 2022 Evaluation of metal additive manufacturing for high-field modular-stellarator radial plates and conductors *Nuclear Materials and Energy* **30** 101149

[6] Torims T, Pikurs G, Gruber S, Vretenar M, Ratkus A, Vedani M, López E and Brückner F 2021 First Proof-of-Concept Prototype of an Additive Manufactured Radio Frequency Quadrupole *Instruments* **5** 35

[7] F42 Committee 2015 *Terminology for Additive Manufacturing - General Principles - Terminology* (ASTM International)

[8] Sinico M, Cogo G, Benettoni M, Calliari I and Pepato A 2019 Influence of Powder Particle Size Distribution on the Printability of Pure Copper for Selective Laser Melting

[9] Siva Prasad H, Brueckner F, Volpp J and Kaplan A F H 2020 Laser metal deposition of copper on diverse metals using green laser sources *Int J Adv Manuf Technol* **107** 1559–68

[10] Singh G, Missiaen J-M, Bouvard D and Chaix J-M 2021 Copper additive manufacturing using MIM feedstock: adjustment of printing, debinding, and sintering parameters for processing dense and defectless parts *Int J Adv Manuf Technol* **115** 449–62

[11] Ren L, Zhou X, Song Z, Zhao C, Liu Q, Xue J and Li X 2017 Process Parameter Optimization of Extrusion-Based 3D Metal Printing Utilizing PW–LDPE–SA Binder System *Materials* **10** 305

[12] Davis J R 2001 *Copper and copper alloys* ed ASM International (Materials Park, OH: ASM International)

[13] Jiang Q, Zhang P, Yu Z, Shi H, Wu D, Yan H, Ye X, Lu Q and Tian Y 2021 A Review on Additive Manufacturing of Pure Copper *Coatings* **11** 740

[14] Roccetti Campagnoli M, Galati M and Saboori A 2021 On the processability of copper components via powder-based additive manufacturing processes: Potentials, challenges and feasible solutions *Journal of Manufacturing Processes* **72** 320–37

[15] Jadhav S D, Vleugels J, Kruth J-P, Humbeeck J V and Vanmeensel K 2020 Mechanical and electrical properties of selective laser-melted parts produced from surface-oxidized copper powder *Material Design & Processing Communications* **2** e94

[16] Wagenblast P, Myrell A, Thielmann M, Scherbaum T and Coupek D 2020 Additive manufacturing with green disk lasers *Laser 3D Manufacturing VII* Laser 3D Manufacturing VII vol 11271 (International Society for Optics and Photonics) p 112710J

[17] Guschlbauer R, Momeni S, Osmanlic F and Körner C 2018 Process development of 99.95% pure copper processed via selective electron beam melting and its mechanical and physical properties *Materials Characterization* **143** 163–70

[18] Yadav S, Paul C P, Jinoop A N, Rai A K and Bindra K S 2020 Laser Directed Energy Deposition based Additive Manufacturing of Copper: Process Development and Material Characterizations *Journal of Manufacturing Processes* **58** 984–97

[19] Huang J, Yan X, Chang C, Xie Y, Ma W, Huang R, Zhao R, Li S, Liu M and Liao H 2020 Pure copper components fabricated by cold spray (CS) and selective laser melting (SLM) technology *Surface and Coatings Technology* **395** 125936

[20] Deshmukh P S, Tomar K, Sathiaraj G D and Palani I A 2022 Optimum strength and ductility of pure copper fabricated by Wire Arc Additive Manufacturing *Manufacturing Letters* **33** 24–8

[21] Yegyan Kumar A, Wang J, Bai Y, Huxtable S T and Williams C B 2019 Impacts of process-induced porosity on material properties of copper made by binder jetting additive manufacturing *Materials & Design* **182** 108001

[22] Zhao Y, Gao W, Xi J, Li H and Ren F 2020 Development of copper powder paste for direct printing and soft mold casting *Additive Manufacturing* **31** 100992

[23] Hutasoit N, Rashid R A R, Palanisamy S and Duguid A 2020 Effect of build orientation and post-build heat treatment on the mechanical properties of cold spray additively manufactured copper parts *Int J Adv Manuf Technol* **110** 2341–57

[24] Williams S W, Rashid A, Pardal G and Quintino L 2019 Wire and arc additive manufacture of highly conducting pure copper *Conference Proceedings* 9

[25] 3D Inductors 2022 How we do it - 3D inductor manufacturing method

[26] Ureña J, Martínez M, Portolés L, Sanjuán S and Blasco J R 2019 Pure copper development at industrial scale by Electron Beam Melting technology VII Congreso Nacional de Pulvimetalurgia y II Congreso Iberoamericano de Pulvimetalurgia p 3

[27] Thomas A, Fribourg G, Blandin J-J, Lhuissier P, Dendievel R and Martin G 2021 Effect of the build orientation on mechanical and electrical properties of pure Cu fabricated by E-PBF *Additive Manufacturing* **48** 102393

[28] Jadhav S D, Goossens L R, Kinds Y, Hooreweder B V and Vanmeensel K 2021 Laser-based powder bed fusion additive manufacturing of pure copper *Additive Manufacturing* **42** 101990

[29] Colopi M, Demir A G, Caprio L and Previtali B 2019 Limits and solutions in processing pure Cu via selective laser melting using a high-power single-mode fiber laser *Int J Adv Manuf Technol* **104** 2473–86

[30] Jadhav S D, Dadbakhsh S, Goossens L, Kruth J-P, Van Humbeeck J and Vanmeensel K 2019 Influence of selective laser melting process parameters on texture evolution in pure copper *Journal of Materials Processing Technology* **270** 47–58

[31] Kaden L, Matthäus G, Ullsperger T, Seyfarth B and Nolte S 2018 Selective laser melting of copper using ultrashort laser pulses at different wavelengths *Laser 3D Manufacturing V* Laser 3D Manufacturing V vol 10523 (International Society for Optics and Photonics) p 1052312

[32] Gruber S, Stepien L, López E, Brueckner F and Leyens C 2021 Physical and Geometrical Properties of Additively Manufactured Pure Copper Samples Using a Green Laser Source *Materials* **14** 3642

[33] Nordet G, Gorny C, Mayi Y, Daligault J, Dal M, Effernelli A, Blanchet E, Coste F and Peyre P 2022 Absorptivity measurements during laser powder bed fusion of pure copper with a 1 kW cw green laser *Optics & Laser Technology* **147** 107612

[34] Hori E, Sato Y, Shibata T, Tojo K and Tsukamoto M 2021 Development of SLM process using 200 W blue diode laser for pure copper additive manufacturing of high density structure *Journal of Laser Applications* **33** 012008

[35] Takenaka K, Sato Y, Tojo K and Tsukamoto M 2021 Development of SLM 3D printing system using Galvano scanner for pure copper additive manufacturing by 200 W blue diode laser Lasers in Manufacturing Conference 2021 p 5

[36] Imai K, Ikeshoji T-T, Sugitani Y and Kyogoku H 2020 Densification of pure copper by selective laser melting process *Mechanical Engineering Journal* **7** 19-00272-19–00272

[37] EOS 2019 EOS Copper Cu

[38] PROTIQ 2021 Material Data sheet - material datasheet laser melting of metals

[39] Bonesso M, Rebesan P, Gennari C, Mancin S, Dima R, Pepato A and Calliari I 2021 Effect of Particle Size Distribution on Laser Powder Bed Fusion Manufacturability of Copper *Berg Huettenmaenn Monatsh* **166** 256–62

[40] Qu S, Ding J, Fu J, Fu M, Zhang B and Song X 2021 High-precision laser powder bed fusion processing of pure copper *Additive Manufacturing* **48** 102417

[41] Gu R N, Chen P, Zhou Y H, Wang H, Yan X C, Wong K S and Yan M 2021 Intentional Oxidation and Laser Remelting of Highly Reflective Pure Cu for Its High-Quality Additive Manufacturing *Adv Eng Mater* 2101138

[42] Jadhav S D, Dadbakhsh S, Vleugels J, Hofkens J, Van Puyvelde P, Yang S, Kruth J-P, Van Humbeeck J and Vanmeensel K 2019 Influence of Carbon Nanoparticle Addition (and Impurities) on Selective Laser Melting of Pure Copper *Materials* **12** 2469

[43] Tertuliano O A, DePond P J, Doan D, Matthews M J, Gu X W, Cai W and Lew A J 2022 Nanoparticle-enhanced absorptivity of copper during laser powder bed fusion *Additive Manufacturing* **51** 102562

[44] Zheng R, Cui J, Yang Y, Li S, Misra R D K, Kondoh K, Zhu Q, Lu Y and Li X 2022 Enhanced densification of copper during laser powder bed fusion through powder surface alloying *Journal of Materials Processing Technology* **305** 117575

[45] Jadhav S D, Fu D, Deprez M, Ramharter K, Willems D, Van Hooreweder B and Vanmeensel K 2020 Highly conductive and strong CuSn0.3 alloy processed via laser powder bed fusion starting from a tin-coated copper powder *Additive Manufacturing* **36** 101607

[46] Jadhav S D, Dhekne P P, Dadbakhsh S, Kruth J-P, Van Humbeeck J and Vanmeensel K 2020 Surface Modified Copper Alloy Powder for Reliable Laser-based Additive Manufacturing *Additive Manufacturing* **35** 101418

[47] Jadhav S D, Dhekne P P, Brodu E, Van Hooreweder B, Dadbakhsh S, Kruth J-P, Van Humbeeck J and Vanmeensel K 2021 Laser powder bed fusion additive manufacturing of highly conductive parts made of optically absorptive carburized CuCr1 powder *Materials & Design* **198** 109369

[48] Jadhav S D, Dadbakhsh S, Chen R, Shabadi R, Kruth J-P, Van Humbeeck J and Vanmeensel K 2020 Modification of Electrical and Mechanical Properties of Selective Laser-Melted CuCr0.3 Alloy Using Carbon Nanoparticles *Adv. Eng. Mater.* **22** 1900946

[49] Steen W M and Mazumder J 2010 *Laser Material Processing* (London: Springer London)

[50] Heider A, Hess A, Weber R and Graf T 2011 Stabilized copper welding by using power modulated green and IR laser beams *International Congress on Applications of Lasers & Electro-Optics* ICALEO® 2011: 30th International Congress on Laser Materials Processing, Laser Microprocessing and Nanomanufacturing (Orlando, Florida, USA: Laser Institute of America) pp 395–402

[51] Demir A G, Colopi M and Previtali B 2019 The use of a ns-pulsed, high repetition rate green laser for SLM of 99.9% pure Cu Lasers in Manufacturing Conference 2019 p 8

[52] Trumpf 2020 Green laser: 3D printing of copper and other precious metals

[53] Desktop Metal 2021 Material Data sheet - pure copper

[54] Digital Metal 2021 Material Data sheet

[55] Markforged 2022 Material datasheet - Copper

[56] Desktop Metal 2020 Material Data sheet - copper

[57] Rodriguez J, Vicente J I, Ezeiza J C, Zuriarrain A, Arrazola P J, Badiola X, Dominguez E and Soler D 2021 Mechanical and electrical properties of additively manufactured copper *IOP Conf. Ser.: Mater. Sci. Eng.* **1193** 012034

[58] Singh G, Missiaen J-M, Bouvard D and Chaix J-M 2021 Copper extrusion 3D printing using metal injection moulding feedstock: Analysis of process parameters for green density and surface roughness optimization *Additive Manufacturing* **38** 101778

[59] Yan X, Wang C, Xiong W, Hou T, Hao L and Tang D 2018 Thermal debinding mass transfer mechanism and dynamics of copper green parts fabricated by an innovative 3D printing method *RSC Adv.* **8** 10355–60

[60] ISO 21920-2:2021 2021 *Spécification géométrique des produits (GPS) — État de surface: Méthode du profil — Partie 2: Termes, définitions et paramètres d'état de surface* (ISO/TC 213)

[61] De Terris T, Andreau O, Peyre P, Adamski F, Koutiri I, Gorny C and Dupuy C 2019 Optimization and comparison of porosity rate measurement methods of Selective Laser Melted metallic parts *Additive Manufacturing* **28** 802–13

[62] E04 Committee 1999 *Practice for Microetching Metals and Alloys* (ASTM International)

[63] Nowell M M, Witt R A and True B 2005 EBSD Sample Preparation: Techniques, Tips, and Tricks *MAM* **11**

[64] Bachmann F, Hielscher R and Schaeben H 2011 Grain detection from 2d and 3d EBSD data—Specification of the MTEX algorithm *Ultramicroscopy* **111** 1720–33

[65] Anon MTEX Toolbox

[66] De Terris T, Castelnau O, Hadjem-Hamouche Z, Haddadi H, Michel V and Peyre P 2021 Analysis of As-Built Microstructures and Recrystallization Phenomena on Inconel 625 Alloy Obtained via Laser Powder Bed Fusion (L-PBF) *Metals* **11** 619

[67] Yamasaki M, Kagao S and Kawamura Y 2005 Thermal diffusivity and conductivity of Zr55Al10Ni5Cu30 bulk metallic glass *Scripta Materialia* **53** 63–7

[68] Strano G, Hao L, Everson R M and Evans K E 2013 Surface roughness analysis, modelling and prediction in selective laser melting *Journal of Materials Processing Technology* **213** 589–97

[69] Tian Y, Tomus D, Rometsch P and Wu X 2017 Influences of processing parameters on surface roughness of Hastelloy X produced by selective laser melting *Additive Manufacturing* **13** 103–12

[70] Hong M-H, Min B and Kwon T-Y 2016 The Influence of Process Parameters on the Surface Roughness of a 3D-Printed Co–Cr Dental Alloy Produced via Selective Laser Melting *Applied Sciences* **6** 401

[71] Wang P, Sin W, Nai M and Wei J 2017 Effects of Processing Parameters on Surface Roughness of Additive Manufactured Ti-6Al-4V via Electron Beam Melting *Materials* **10** 1121

[72] King W E, Barth H D, Castillo V M, Gallegos G F, Gibbs J W, Hahn D E, Kamath C and Rubenchik A M 2014 Observation of keyhole-mode laser melting in laser powder-bed fusion additive manufacturing *Journal of Materials Processing Technology* **214** 2915–25

[73] Raab S J, Guschlbauer R, Lodes M A and Körner C 2016 Thermal and Electrical Conductivity of 99.9% Pure Copper Processed via Selective Electron Beam Melting: Conductivities of Pure SEBM-Copper *Adv. Eng. Mater.* **18** 1661–6

[74] Cañadilla A, Romero A, Rodríguez G P, Caminero M Á and Dura Ó J 2022 Mechanical, Electrical, and Thermal Characterization of Pure Copper Parts Manufactured via Material Extrusion Additive Manufacturing *Materials* **15** 4644

[75] Kou S 2003 *Welding metallurgy* (Hoboken, N.J: Wiley-Interscience)

[76] Ternero F, Rosa L G, Urban P, Montes J M and Cuevas F G 2021 Influence of the Total Porosity on the Properties of Sintered Materials—A Review *Metals* **11** 730

[77] Chapman D 2016 High Conductivity Copper for Electrical Engineering 32

[78] Çetinarslan C S 2009 Effect of cold plastic deformation on electrical conductivity of various materials *Materials & Design* **30** 671–3